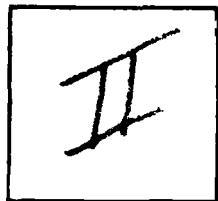
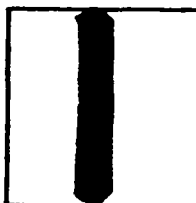


ADA137753

PHOTOGRAPH THIS SHEET



LEVEL



INVENTORY

DTIC ACCESSION NUMBER

Kinetics of Rare Gas Halide and Mercury  
Halide Lasers

FINAL REPORT

DOCUMENT IDENTIFICATION

REPORT PERIOD Jan. 1, 1980 - Dec. 31, 1980

CONTRACT No. N00014-76-C-380

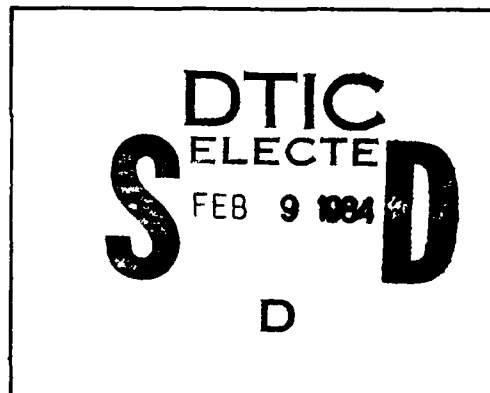
DISTRIBUTION STATEMENT A

Approved for public release;  
Distribution Unlimited

DISTRIBUTION STATEMENT

ACCESSION FOR	
NTIS	GRA&I
DTIC	TAB
UNANNOUNCED	
JUSTIFICATION	
BY Per Ltr. on file	
DISTRIBUTION /	
AVAILABILITY CODES	
DIST	AVAIL AND/OR SPECIAL
A/I	

DISTRIBUTION STAMP



DATE ACCESSIONED

83 11 29 041

DATE RECEIVED IN DTIC

PHOTOGRAPH THIS SHEET AND RETURN TO DTIC-DDA-2

NR 395-553 ADW  
Logged 4/1/81 CA

Kinetics of Rare Gas Halide and Mercury  
Halide Lasers

FINAL REPORT

REPORT PERIOD Jan. 1, 1980 - Dec. 31, 1980

CONTRACT No. N00014-76-C-380

ARPA Order No. - 2840, Amendment No. 12

AD A 137753

from

KANSAS STATE UNIVERSITY

Department of Chemistry  
Kansas State University  
Manhattan, Kansas 66506

Effective Date of Contract Jan. 1, 1979 - Dec. 31, 1979  
Extended Date Jan. 1, 1980 - Dec. 31, 1980  
Amount of Contract \$43,000  
Amount of Supplement \$11,000

ARPA Contract No. N00014-76-C-380

Modification P0003

MECHANISMS, BRANCHING RATIOS AND RATE CONSTANTS  
FOR EXCITATION PROCESSES IN RARE GAS SYSTEMS

Principal Investigator: D. W. Setser  
Phone No. 913-532-6692

Scientific Officer: Director, Physics  
Physical Science Division  
Office of Naval Research

Sponsored by

Advanced Research Projects Agency  
ARPA Order No. 2840

DISTRIBUTION STATEMENT A  
Approved for public release  
Distribution Unlimited



11-18-81

DEPARTMENT OF THE NAVY  
OFFICE OF NAVAL RESEARCH BRANCH OFFICE CHICAGO  
536 S. CLARK STREET  
CHICAGO, ILLINOIS 60605

IN REPLY REFER TO:  
ONR-Chi/GRT:ldg  
Kansas State Univ./  
N00014-76-C-0380  
(NR 395-553)  
5 November 1981

From: Office of Naval Research Branch Office Chicago  
To: Chief of Naval Research (Code 421)

Subj: Certificate of completion of technical performance under Contract N00014-76-C-0380 (NR395-553) with Kansas State University

Ref: KSU/D.W. Setser report of 31 Dec 1980

1. The final technical report under the subject contract was submitted to the addressee by reference (a).
2. This office is currently in the process of closing out the subject contract. It is requested that the certificate below be executed, if appropriate, and that two signed copies thereof be returned to this office as soon as practicable in order that further closeout actions and processing of the completion voucher will not be unduly delayed.

*Glen R. Timmerman*  
GLEN R. TIMMERMAN  
Contract Administrator

---

FIRST ENDORSEMENT on ONR-BrOff Chicago ltr dated 5 November 1981

From: Chief of Naval Research (Code 421)  
To: Office of Naval Research Branch Office Chicago

1. Returned.
2. The undersigned hereby certifies that the subject Contractor has completed the technical performance required under the subject contract or grant.

*Allyn A. O'Neil* 11-18-81  
Scientific Officer Date

Final Report for One Year Extension

Mr. Trecil Dreiling worked full time and Dr. David Wren for a short time on this contract. Mr. Dreiling completed the modeling calculations for vibrational and electronic state relaxation processes of XeCl(B,C) in rare gas buffers. A manuscript describing the work is attached. A paper describing some of Dr. Wren's studies also is attached. The principal investigator also has written several other papers describing work completed with prior support of this contract. Our efforts are now finished and all the work has been submitted for publication. All financial transactions also are completed and the University is closing this account.

Answers to specific questions listed in the suggested format for the Status Report are given below:

- a) Research Program Plans . . . . . Completed
- b) Equipment Purchase . . . . . None
- c) Personnel Changes . . . . . See above
- d) Meetings/Conferences . . . . . Attended Gaseous Electronic Conference in Norman, OK
- e) Actions Required by ARPA or ONR . . . . . None
- f) Achievement of Objectives . . . . . Project completed

D. W. Setser

# Fluorescence of Optical Materials Stimulated by ArF Laser Radiation at 193 nm

DAVID J. WREN\*

Department of Chemistry, Kansas State University, Manhattan, Kansas 66506

The fluorescence spectra of four optical materials (S1-UV quartz, UV grade sapphire,  $MgF_2$ , and  $BaF_2$ ) have been recorded using ArF laser radiation at 193 nm (6.4 eV) as an excitation source. The time-resolved fluorescence intensities have also been measured at several wavelengths using a transient digitizer with 2 ns resolution. All of the materials exhibit a fast fluorescence which follows the exciting laser pulse and has a lifetime  $\tau_R < 7 \pm 2$  ns. This fast fluorescence is present as a broad continuum from 200 to 1000 nm with maxima in the UV and the IR. In addition, there are fluorescence components with longer lifetimes which are characteristic of the individual materials. The results suggest further opportunities for study of optical materials using ArF lasers and indicate an area of caution to be exercised by experimentalists employing ArF lasers for excitation experiments.

Index Headings: ArF laser; Laser-induced fluorescence; Optics; Time-resolved spectroscopy.

## INTRODUCTION

The recent advent of the rare gas halide lasers has provided experimentalists with a valuable new source of intense UV radiation.<sup>1</sup> With peak radiance powers on the order of  $10^6$  W and pulse durations of 10 ns, they are ideal radiation sources for a variety of work including photolytic reactions,<sup>2</sup> multiphoton ionization,<sup>3,4</sup> two photon excitation of high electronic states,<sup>5</sup> and fast kinetics initiated by absorption of one or more photons. Despite the body of work employing these lasers which has been published, there has been no mention in the literature of the effects of the RgX laser radiation on optical materials. For many of the above experiments and particularly the last, interference from laser-stimulated fluorescence in optical materials can be an important factor. In this paper we report fluorescence spectra observed from four optical materials stimulated by ArF laser radiation at 193 nm (6.4 eV).

The materials studied here are: S1-UV grade quartz, UV grade sapphire,  $MgF_2$ , and  $BaF_2$ . All of these materials are considered suitable optical materials at 193 nm and are not noted for fluorescence in the presence of UV radiation. However, all four materials are observed to fluoresce with different spectra and fluorescence lifetimes. The fluorescence observed from quartz is particularly severe. The generation of fluorescence by intense radiation from an ArF laser is not particularly surprising, but can pose problems for the experimentalist who wishes to observe light from a reaction or other process initiated by an ArF laser.

The intention of this work is to report the fluorescence

spectra observed for the above materials, particularly as a guide to other experimentalists. The discussion of the results is limited in scope, and we do not attempt to identify the mechanism or states responsible for the fluorescence observed.

## I. EXPERIMENTAL

A schematic diagram of the experiment is shown in Fig. 1. The laser source was a Lumonics TE-261 rare gas halide laser operating on the ArF 193 nm lasing transition using a mixture of 20% Ar, 0.4% F<sub>2</sub>, and 79.6% He at a total pressure of 1500 Torr. The gases were: Matheson prepurified Ar (99.998%), Matheson technical grade F<sub>2</sub> (>97%) as 10% F<sub>2</sub> in He, and high purity He (99.995%). The laser was operated in the static fill mode with the mixtures prepared by backfilling the laser using a Tachisto model GMS 150 gas handling system. At 44 kV and 5 Hz the laser yielded an initial energy of ~100 mJ/pulse with an approximately linear decrease in energy with the number of pulses to ~50 mJ/pulse after ~2500 pulses. Pulse to pulse stability was  $\pm 5\%$ . The laser mixture was normally renewed after ~2400 pulses. The full width of half maximum of the laser profile was measured to be 123 cm<sup>-1</sup> and the laser pulse width was 14  $\pm 2$  ns.

The materials used in this study were: (a) an S1-UV quartz flat, 25 mm diameter, 3 mm thick, supplied by Esco Products; (b) a UV grade sapphire flat 18 mm diameter, 1 mm thick, supplied by Adolf Meller; (c) a  $MgF_2$  flat, 25 mm diameter, 1 mm thick, supplied by Harshaw; and (d) a  $BaF_2$  lens, 50 mm diameter, 3 mm thick, f/12, supplied by Harshaw. The optical materials were mounted at an angle of ~30°, 70 cm along the path of the laser beam. At this point the laser beam cross section is 25 mm by 6 mm. Specular reflection was directed away from the entrance slit of the monochromator, and a light shield prevented radiation from the laser directly entering the monochromator. Non-specular scattering of the laser light remains sufficiently intense to appear at higher orders in the fluorescence spectra. Fluorescence from the irradiated materials was collected by a 50 mm f/1 quartz lens and focused onto the entrance slit of the monochromator.

The fluorescence spectra were scanned using a 0.3 m McPherson monochromator equipped with a grating blazed at 300 nm, 1200 g/mm for wavelengths 200 to 600 nm, and a grating blazed at 1000 nm, 1200 g/mm for wavelengths 600 to 1000 nm. The light was detected by an RCA 31034 photomultiplier tube cooled to -20°C in a Products for Research rf shielded housing. The current generated by the phototube was passed directly via 1 m of coaxial cable to the 50 Ω input of a Biomation transient digitizer. The Biomation has a 1024 channel time base with a minimum sample interval of 2 ns and a resolution

Received 20 May 1980.

\* Present address: Atomic Energy of Canada, Whiteshell Nuclear Research Station, Pinawa, Manitoba, Canada R0E 1L0.

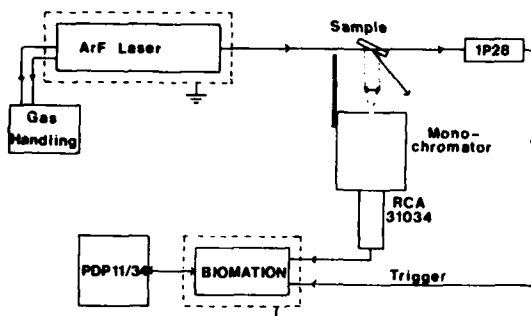


FIG. 1. A schematic diagram of the experimental apparatus for measurement of ArF laser induced fluorescence.

of 6 bits for each channel. Triggering for the Biomation was provided by an RCA 1P28 multiplier which viewed the laser beam directly via a pinhole. Driven at very low voltage (~200 V) the photomultiplier tube signal was sufficient to trigger the Biomation on the leading edge of the laser pulse and the electronics were operated in a delayed trigger mode with 0 delay time. Biomation trigger jitter was  $\pm 6$  ns at the fastest sample rate. Both the Biomation and the ArF laser were enclosed in grounded Faraday cages made of copper mesh, and the Biomation power supply was isolated by a line filter. These precautions were necessary to reduce rf interference generated by the laser spark gap and gas discharge. Random and systematic rf noise were reduced to an acceptable level but not completely eliminated.

The Biomation was controlled by a PDP 11/34 computer which stored the waveform generated by each pulse and performed required data handling. In measuring the time dependence of the fluorescence at a particular wavelength, typically 200 waveforms were acquired and averaged, and a background subtraction performed to remove the rf noise. The fluorescence spectra were recorded by using the Biomation and computer as a boxcar integrator. For each spectral point the computer acquired 10 waveforms from the Biomation, averaged them, subtracted the rf background and integrated the result over a pre-selected time interval of the waveform. The monochromator was scanned continuously at 50 nm/min and the data points collected were 2.5 nm apart. The monochromator slit width was 1 mm corresponding to a resolution of 2.6 nm. Lack of synchronism between computer and monochromator, because they were not interfaced, resulted in an error of  $\pm 10$  nm after scanning 400 nm. Since the fluorescence spectra are primarily continua, this is not a serious problem.

Since the laser was operated in a static fill mode, the intensity of the laser decayed during the time required for a spectrum to be obtained. Furthermore, the laser mixture was replaced when the gratings were changed at 600 nm. The dependence of the fluorescence intensity on the intensity of the laser radiation was measured for all of the samples. The method was simply to follow the integrated fluorescence intensity at a particular wavelength as the laser intensity decayed. The result in all cases found the fluorescence intensity to be first order in the laser intensity. All of the spectra which appear here have been corrected for the decay in the laser intensity using this result. The spectra have not been corrected for

the wavelength dependent response of the detection system.

## II. RESULTS

**A. S1-UV Quartz.** S1-UV quartz exhibits the most intense fluorescence of the four materials examined. To the eye, the quartz flat gives off a bright blue-white light when struck by the ArF laser beam. The relative intensity of the quartz fluorescence at 400 nm, time integrated from 0 to 2000 ns, is compared to that of the other materials in Table I. The quartz emission is ~40 times stronger than the others, which all have comparable fluorescence intensities. The relative intensities are wavelength dependent, and, in general, the quartz is always by far, the strongest. The blue fluorescence of the quartz flat may explain the observation that the ArF laser beam from the Lumonics laser is visible to the eye as bright blue, despite the fact that the lasing occurs in the UV. The light is likely due to the fact that the output coupler of this laser is made of quartz.

The fluorescence spectrum of S1-UV quartz is shown in Fig. 2. The intensity recorded by each point represents the time-integrated fluorescence from 0 to 2000 ns. The spectrum consists of a broad continuum from 200 to 1000 nm with maxima at 300 nm and at 950 nm. Several

TABLE I. Relative fluorescence intensities.

Material	$I_{REL}^{a,b}$
S1-UV quartz	1.0
Sapphire	$0.023 \pm 0.005^c$
$MgF_2$	$0.022 \pm 0.004^c$
$BaF_2$	$0.030 \pm 0.006^c$

<sup>a</sup> Normalized to S1-UV quartz.

<sup>b</sup>  $\lambda = 400$  nm, fluorescence integrated from 0 to 2000 ns.

<sup>c</sup> Error limits are  $\pm 0.002$  for the measured data. Differences in the geometries of the irradiated samples could not be accounted for exactly and an overall error in the relative intensities of 20% is estimated.

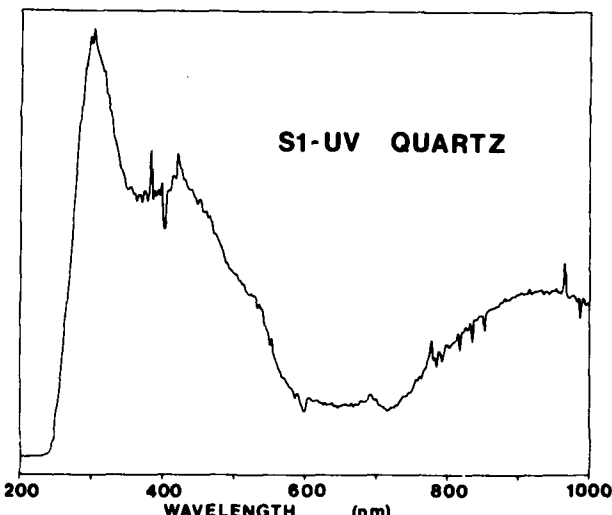


FIG. 2. Spectrum of the fluorescence from an irradiated S1-UV quartz sample. Fluorescence is time integrated from 0 to 2000 ns. Resolution is 2.6 nm. The narrow features at 386, 772, and 965 nm are scattered ArF laser light in second, fourth, and fifth order. The line in third order at 579 nm is too weak to observe. Spectrum is corrected for variation in laser intensity, but not for wavelength response of detector.

narrow features are due to scattered ArF laser radiation in second to fifth order. The decay of the quartz fluorescence intensity at 300 nm is plotted against time in Fig. 3. The curve exhibits an initial fast decay with a decay time of  $16 \pm 2$  ns and a second much slower decay with a decay time of  $450 \pm 40$  ns. The decay times quoted for this fluorescence and all decay times later quoted were determined by logarithmic least square fits to the data over a range where a logarithmic plot of the intensity vs time is linear. No fit was made with fewer than 10 data points and for long decays several hundred points were used. The error limits quoted are to 1 standard deviation in the slopes of the logarithmic lines fit to the data. The fluorescence decay measured at all wavelengths contains both a fast (0 to 40 ns) and slow (40 to 2000 ns) component with variation in relative intensities of the fast and slow light and with the decay lifetime of the slow emission varying from 173 to 556 ns. The slow emission present at all wavelengths contributes the dominant fraction of the time integrated fluorescence intensity and hence the spectrum in Fig. 2 is primarily that of the slow emission. No attempt was made to separate the fast and slow components over 0 to 40 ns in order to obtain a spectrum of just the fast emission component. The dependence of the fluorescence intensity on the intensity of the laser source was measured for both the combined fast and slow components integrated over 0 to 2000 ns and the slow component alone integrated over 40 to 2000 ns. The results for both cases found the fluorescence to be first order in the ArF laser intensity independent of wavelength.

**B. Sapphire.** The sapphire fluorescence spectrum is shown in Fig. 4. It is similar to that from quartz in that the spectrum is a continuum from 200 to 1000 nm with maxima in the blue at 325 nm and in the red at 975 nm and also contains ArF laser lines. These lines appear more intense than in Fig. 2, due to the lower intensity of the sapphire fluorescence. The photomultiplier sensitivities used to record the spectra for sapphire, BaF<sub>2</sub>, and MgF<sub>2</sub> were higher than that used for the quartz spectrum.

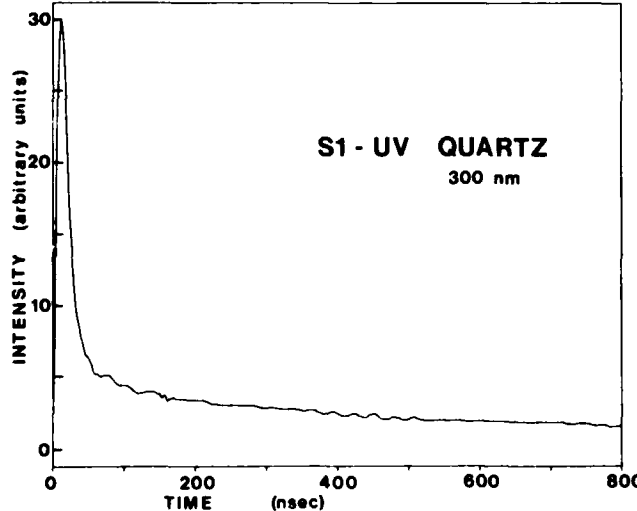


FIG. 3. Fluorescence intensity at 300 nm as a function of time from irradiated S1-UV quartz. The decay time of fast fluorescence is  $14 \pm 2$  ns and the decay time of the slow fluorescence is  $450 \pm 40$  ns.

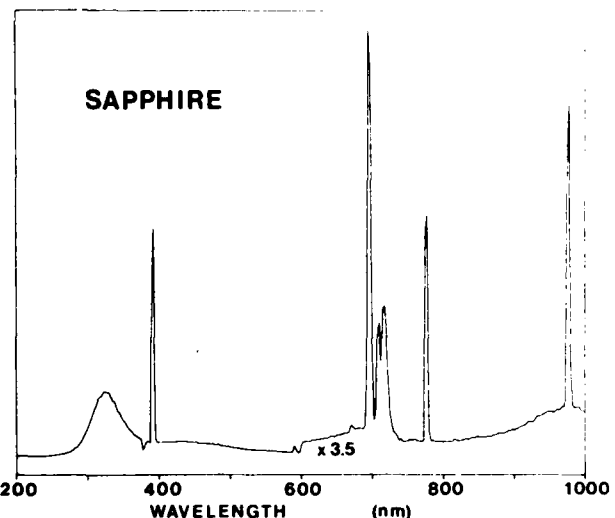


FIG. 4. Spectrum of the fluorescence from an irradiated UV-grade sapphire sample. Fluorescence is time integrated from 0 to 2000 ns. The narrow features at 386, 579, 772, and 965 nm are scattered ArF laser light in second, third, fourth, and fifth order. Spectrum is corrected for variation in the laser intensity but not for wavelength response of detector.

As a result the ArF line in higher orders saturates the detection system and appears off scale. The intensities of the ArF lines appearing in the spectra of Figs. 4, 6, and 7 are not accurate but give a qualitative guide to the relative intensities of the fluorescence spectra. A unique feature of the sapphire spectrum is a group of narrow bands around 700 nm. These bands are responsible for the bright red fluorescence of this material, which is visible to the eye.

Unlike the S1-UV quartz, the sapphire fluorescence spectrum is primarily due to a fast emission process. The light intensity at 300 nm plotted as a function of time is shown in Fig. 5a. The fast emission follows the laser pulse even more closely than in quartz with a decay time of  $7 \pm 2$  ns. Similar decay curves are observed at other wavelengths except those spanned by the red bands. These bands arise from a much different fluorescence process and have a very long decay lifetime. The fluorescence intensity as a function of time for emission at 694.5 nm is shown in Fig. 5b. This emission reaches a maximum  $0.6 \pm 0.2$  ms after the laser pulse and decays with a lifetime of  $1.1 \pm 0.2$  ms. The intensities of both the continuum fast fluorescence and the slow fluorescence of the red bands were found to be first order in the intensity of the ArF laser intensity.

**C. MgF<sub>2</sub>.** To the eye, the fluorescence of MgF<sub>2</sub> is the weakest of all the materials studied. There is only a faint blue-purple emission visible when irradiated by the ArF laser. The fluorescence of MgF<sub>2</sub> like that of sapphire is dominated by a fast decay component similar to that shown in Fig. 5a. This emission again follows the laser pulse shape closely with a decay time of  $7 \pm 2$  ns and is present at all wavelengths. The fluorescence spectrum of this fast emission alone is shown in Fig. 6a where the intensity was integrated only over the light emitted from 0 to 40 ns. The basic features of the spectrum are similar to those of sapphire except for an additional maximum in the UV. The fluorescence of the band at 300 nm is

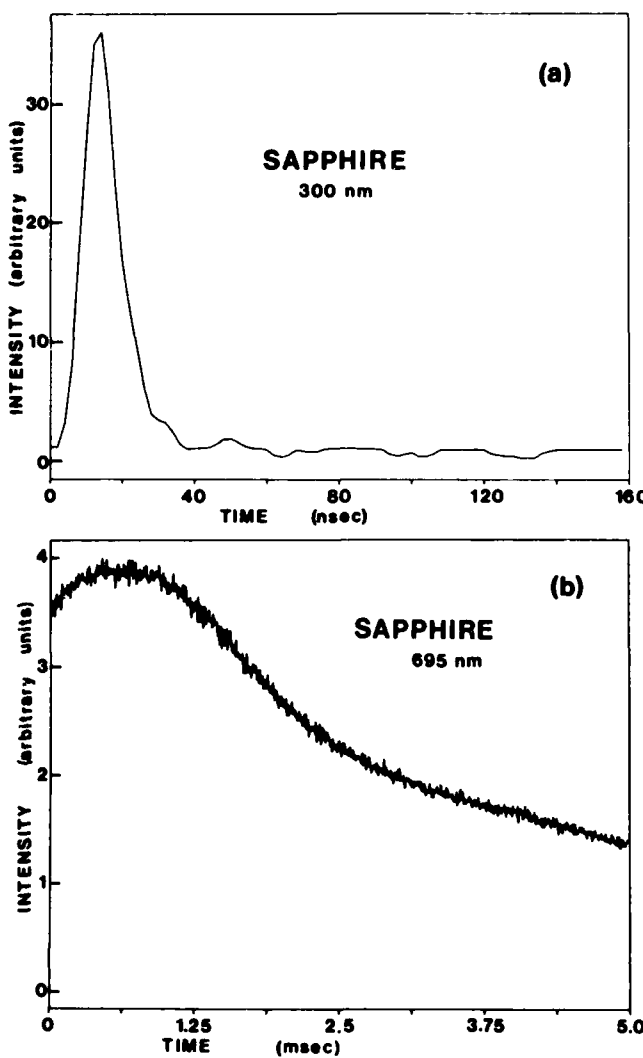


FIG. 5. a. Fluorescence intensity at 300 nm as a function of time for irradiated sapphire. b. Fluorescence intensity at 694.5 nm as a function of time for irradiated sapphire. Note the change in scale of the time axis compared to Fig. 5a.

complicated by the addition of a second component with a decay lifetime of  $32 \pm 2$  ns.

The fast emission from  $MgF_2$  is much more intense than the slow emission and dominates a time-integrated spectrum. However, there is a weak slow decay fluorescence with a lifetime ranging from 400 to 495 ns depending on the wavelength. The fluorescence spectrum of this slow emission is shown in Fig. 6b where a trigger delay on the Biomation acquisition has removed the fast light (0 to 40 ns), and the intensity is time-integrated from 40 to 2040 ns. The dominant feature of this spectrum is a maximum at 307.5 nm corresponding to the shortest wavelength UV maximum of the spectrum shown in Fig. 6a. Also present are very strong lines from the scattered ArF laser line. These are present here despite the trigger delay because the detection system has not yet recovered from the saturation by the intense signal. Very weak features are present near 800 nm. The band at 812.5 nm has a decay similar in shape to the 694.5 nm band of sapphire but reaches a maximum in intensity at  $0.8 \pm 0.2$   $\mu$ s and decays with a lifetime of  $2.1 \pm 5$   $\mu$ s.

**D.  $BaF_2$ .** The spectrum for the fluorescence of  $BaF_2$  is shown in Fig. 7 for light intensity integrated from 0 to 2000 ns. Visibly the  $BaF_2$  fluoresces with a faint red color that is much less intense than the sapphire. The decay curves for the fluorescence are very similar to those of  $MgF_2$ . At all wavelengths, except for the continuum band around 300 n, a fast emission with decay time  $7 \pm 2$  ns dominates. The 300 nm band derives from a slow emission with a decay time of  $\sim 30$  ns which contributes  $\sim 50\%$  of the intensity of the double peaked band.

### III. DISCUSSION

The experimental results demonstrate that ArF laser radiation is particularly efficient at stimulating fluorescence in many and possibly all optical materials. The case of quartz is particularly outstanding. For this ma-

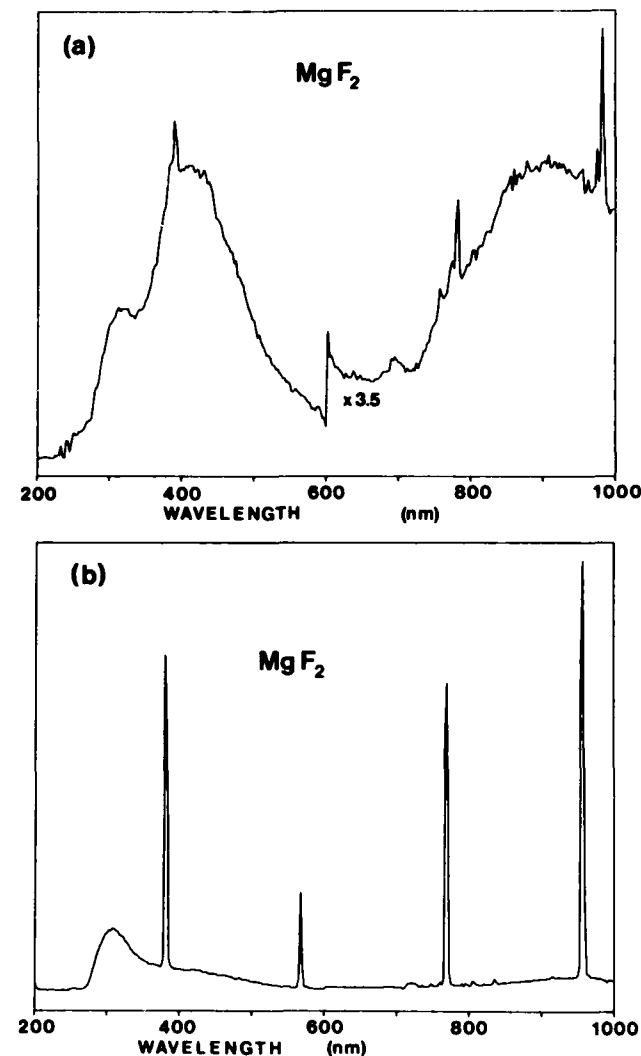


FIG. 6. a. Spectrum of the fluorescence from an irradiated  $MgF_2$  sample. Fluorescence is time integrated from 0 to 40 ns. The narrow features at 386, 772, and 965 nm are scattered ArF laser light in second, fourth, and fifth order. Spectrum corrected for variation in laser intensity but not for wavelength response of detector. b. Spectrum of fluorescence from an irradiated  $MgF_2$  sample. Fluorescence time integrated from 40 to 2040 ns. Note the much higher relative intensity of the ArF lines compared to Fig. 6a. Spectrum corrected for variation in laser intensity but not for wavelength response of detector.

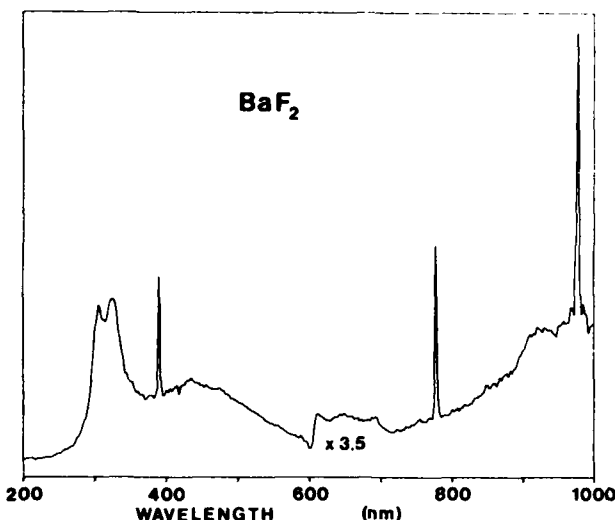


FIG. 7. Spectrum of fluorescence from an irradiated  $\text{BaF}_2$  sample. Fluorescence time integrated from 0 to 2000 ns. The narrow features at 386, 772, and 965 nm are scattered ArF light in second, fourth, and fifth order. Spectrum corrected for variation in laser intensity but not for wavelength response of detector.

terial the blue-white fluorescence is quite bright to the naked eye. While it is well known that most fused silicas fluoresce strongly in the blue when exposed to UV light, the purest grades of fused quartz, including the sample used here, have in the past shown no fluorescence when exposed to conventional forms of UV light.<sup>6</sup> An exception is the observation of a strong emission band at 430 nm observed for both crystalline quartz and fused silica when the samples are cooled to liquid nitrogen temperature and exposed to light at 295 nm.<sup>6</sup> The strong fluorescence observed here where none is expected underlines the efficacy of the ArF laser.

The fluorescence with the slow decay lifetime ~200 to 500 ns observed for the irradiated quartz is likely due to impurities in the material. Virtually all of the luminescent centers in silicate glasses have been traced to the presence of impurities, primarily rare earth and transition metals.<sup>7</sup> Sigel<sup>6</sup> has suggested that the absence of fluorescence previously noted for high purity silicas is related to the fact that well known luminescent activators such as copper, manganese, and silver are present in less than 50 ppb.<sup>8</sup> At the high power densities of the rare gas halide lasers, however, such low impurity levels may no longer be sufficient to reduce the fluorescence. There are high purity grades of silica other than that studied here, which have even lower metal contents (e.g., Suprasil-W, Amerasil, Inc.) and which may exhibit less fluorescence.

The fluorescence spectrum of the sapphire sample is composed of light with a very short lifetime except for the narrow bands in the red. The fast fluorescence can be traced to F and  $\text{F}^+$  centers. Crystalline sapphire is known to have absorption bands at 6.1 and 6.0 eV which have been assigned to these centers.<sup>9, 10</sup> These absorption bands are conveniently close to the ArF laser energy 6.4 eV. An F center emission band at 413 nm (3 eV) has been observed with a lifetime of  $36 \pm 4$  ns<sup>9</sup> which we do not observe. However, Evans and Stapelbroek<sup>10</sup> have reported a 326 nm (3.8 eV) emission which they assign to the  $\text{F}^+$  center and for which they measure a lifetime of

$\tau_R \leq 7$  ns. This agrees very well with the present observation of a fluorescence band at 325 nm with radiative lifetime  $\tau_R = 7 \pm 2$  ns.

No attempt will be made to assign the fluorescence observed for the two alkaline earth fluorides  $\text{MgF}_2$  and  $\text{BaF}_2$ . The fact that most of the fluorescence observed for these two materials has a decay time equivalent to the fast fluorescence observed for sapphire however suggests that F center or  $\text{F}^+$  center transitions may be responsible.

The long fluorescence lifetimes of the red bands near 700 nm in sapphire ( $\tau_R = 1.1 \pm 0.2$  ms) with the band at 812.5 nm in  $\text{MgF}_2$  ( $\tau_R = 2.1 \pm 5$   $\mu\text{s}$ ) suggest that they are of very different origin and possibly metal atom lattice impurities. It is interesting to note that the maxima of these emissions occur long after the laser pulse has been completed ( $0.6 \pm .2$  ms and  $0.8 \pm 0.2$   $\mu\text{s}$ , respectively). This requires the existence of a dark long-lived intermediate state or some energy pooling mechanism.

A feature common to all of the spectra is a maximum in the fluorescence in the IR near 950 nm. The maximum is actually an artifact since the spectra are not corrected for wavelength response. The sensitivity of the RCA 31034 photo-tube decreases very rapidly near 900 nm (at 900 nm the response is  $10^{-2}$  times that at 800 nm), and the mere observation of a signal above 900 nm indicates that the actual fluorescence is very intense and may extend far into the IR.

A final observation is that the fluorescence intensity for all four materials was first order in the ArF laser intensity. This means that no multiphoton absorption events were responsible for the fluorescence. At the high power density of the ArF laser, occurrence of a two photon event is not unreasonable and, moreover, would involve 12.9 eV, energy sufficient to generate color centers in all materials except LiF. The absence of such events noted here may not hold for experiments where the laser beams are focused to provide even higher power densities. Color centers generated by multiphoton events may result in long-lived or permanent coloration of the material.

The fluorescence data reported here are specific to the optical samples studied and may be expected to vary depending on the purity of the material. However, in the cases of sapphire,  $\text{MgF}_2$ , and  $\text{BaF}_2$  where most of the fluorescence decays very rapidly and is probably due to unavoidable lattice defects, variations in sample purity should not change the overall fluorescence spectra. A second factor for consideration affecting the fluorescence is the past history of the optical material. A second sapphire flat which had undergone prolonged exposure to radiation from a Xe resonance lamp (147 nm) in our laboratory was also examined. This window, which had no visible discoloration or damage, fluoresced a very intense blue-violet with a decay time of seconds when exposed to ArF radiation. The experimental results presented here are only a guide to what may be expected for quartz, sapphire,  $\text{BaF}_2$ , and  $\text{MgF}_2$ .

#### IV. CONCLUSION

The preceding discussion has been very brief and makes no attempt to explain most of the observed flu-

rescence features with any rigor. This study was not an exhaustive time-dependent analysis of ArF laser stimulated fluorescence; however, it clearly demonstrates that the ArF laser generates considerable fluorescence in most, if not all, optical materials. The unwary experimenter is forewarned that this fluorescence may cause serious difficulties, particularly in the case of quartz, when studying reactions by optical methods on time scales of nanoseconds.

The efficiency of the ArF laser in exciting fluorescence in optical materials suggests that it may be a very useful tool for studying the optical properties of such materials, as well as such related properties as photoconductivity. The pulse duration of the ArF laser is short enough to allow study of lifetimes for fluorescence down to the nanosecond region. Much more work remains to be done to fully understand the events occurring when an optical material is irradiated at 6.4 eV with megawatt power.

#### ACKNOWLEDGMENTS

This work was supported by the U.S. Department of Energy (AGO 505) and by the Advanced Research Projects Agency of the U.S. Department of Defense

(monitored by ONR-N00014-76-C-0380). The support and advice of D. W. Setser, in whose laboratory this work was carried out, are gratefully acknowledged.

1. a. S. K. Searles and G. A. Hart, *Appl. Phys. Lett.* **27**, 243 (1975).  
b. C. A. Brau and J. J. Ewing, *Appl. Phys. Lett.* **27**, 435 (1975).  
c. E. R. Ault, R. S. Bradford Jr., and M. L. Braumik, *Appl. Phys. Lett.* **27**, 413 (1975).  
d. J. J. Ewing and C. A. Brau, *Appl. Phys. Lett.* **27**, 350 (1975).  
e. J. A. Mangano and J. H. Jacob, *Appl. Phys. Lett.* **27**, 495 (1975).  
f. G. C. Tisone, A. K. Hayes, and J. M. Hoffman, *Opt. Commun.* **15**, 188 (1975).
2. a. W. K. Bischel, G. Black, R. T. Hawkins, D. J. Kligler, and C. K. Rhodes, *J. Chem. Phys.* **70**, 5589 (1979).  
b. W. K. Bischel, J. Bokor, J. Dallarosa, and C. K. Rhodes, *J. Chem. Phys.* **70**, 5593 (1979).  
c. J. J. Tee, F. B. Wampler, and W. W. Rice, *J. Chem. Phys.* **72**, 2914 (1980).  
d. J. Bokor, J. Zavelovich, and C. K. Rhodes, *J. Chem. Phys.* **72**, 967 (1980).
3. a. C. A. Brau, in *Excimer Lasers*, C. K. Rhodes, Ed. (Springer Verlag, New York, 1979), Chap. 4.  
b. C. K. Rhodes and P. W. Hoff, Chap. 6.
4. S. Roekwood, J. P. Reilly, K. Hohla, and K. L. Kompa, *Opt. Commun.* **28**, 175 (1979).
5. W. K. Bischel, J. Bokor, D. J. Kligler, and C. K. Rhodes, *IEEE J. Quantum Elec.* **QE-15**, 380 (1979).
6. G. H. Sigel, *J. Non-Crys. Solids* **13**, 372 (1973).
7. G. E. Rindown, *Luminescence of Inorganic Solids Gases* (Academic Press, New York, 1966), p. 419.
8. G. Hetherington and L. W. Bell, *Phys. Chem.* **8**, 206 (1967).
9. K. H. Lee and J. H. Crawford, *Phys. Rev.* **B19**, 3217 (1979).
10. B. D. Evans and M. Stapelbroek, *Phys. Rev.* **B18**, 7089 (1978).

STATE-TO-STATE RELAXATION PROCESSES FOR XeCl(B,C)

T. D. Dreiling and D. W. Setser

Chemistry Department  
Kansas State University  
Manhattan, Kansas 66506

Received:

ABSTRACT

The XeCl(B-X) and (C-A) emission spectra obtained from reaction of  $\text{Xe}({}^3\text{P}_2 \text{ or } {}^3\text{P}_1)$  with  $\text{Cl}_2$ ,  $\text{CCl}_4$ , and  $\text{COCl}_2$  in the presence of He, Ne, Ar, Kr and  $\text{N}_2$  bath gases were used to study the vibrational relaxation and transfer between the B and C states of XeCl. By using the different Cl donors different ranges of vibrational energy were emphasized. The bound-free emission spectra were simulated for various pressures of bath gas to obtain vibrational distributions. Numerical modeling of the XeCl(B) and XeCl(C) vibrational populations and the B/C intensity ratio as a function of pressure gave rate constants for vibrational relaxation and transfer, as well as the model for the state-to-state processes. For Ar as the bath gas, vibrational relaxation can be characterized by an exponential gap model,  $P_{ij} \propto e^{-0.1 \Delta E/kT}$ , with rate constants of  $1-6$ ,  $6-12$ , and  $20-30 \times 10^{-11} \text{ cm}^3 \text{ molec}^{-1} \text{ sec}^{-1}$  for the v ranges of  $0-30$ ,  $30-70$ , and  $70-130$ , respectively. The rate constants for electronic state transfer are  $3-11$ ,  $11-15$ , and  $15-15 \times 10^{-11} \text{ cm}^3 \text{ molec}^{-1} \text{ sec}^{-1}$  for the same v ranges. The vibrational energy loss upon electronic state transfer was best described by a Poisson type function displaced to lower energy from the initial energy. These basic models also describe the relaxation in the other gases with He and Ne being less efficient and Kr and  $\text{N}_2$  more efficient than Ar. The magnitudes of the rate constants and the models are discussed.

## I. INTRODUCTION

Because of the importance of rare gas halide excimer lasers, considerable research has been directed toward characterizing and understanding the basic kinetic processes of formation, quenching, electronic state transfer, and vibrational relaxation of the B(1/2) and C(3/2) states of the rare gas halide molecules.<sup>1</sup> The importance of the C state has only recently been realized. In fact, the C-A transition of XeF has been made to lase.<sup>2</sup> Clearly the C state must be included in any realistic model of the laser medium and understanding the B-C state coupling and the associated vibrational relaxation may be of importance in optimizing the design and performance of the rare gas halide lasers.

Previous reports from this and other laboratories have provided information concerning the reactions of the first excited states, Rg( $^3P_{2,1}$ ), of the rare gas atom with halogen donating molecules to form the RgX(B,C) molecules. Quenching rate constants and branching fractions have been reported for Ar( $^3P_2$ ), Kr( $^3P_2$ ), and Xe( $^3P_2$ ) with a variety of halogen donors.<sup>3-4</sup> In addition, the bound-free emission spectra from the RgX(B-X) and RgX(C-A) transitions have been interpreted to provide information concerning the vibrational energy disposal and dynamical features of these reactions.<sup>5,6</sup> Although most of the work has been concerned with the metastable  $^3P_2$  state, results for the  $^3P_1$  state appear quite similar.<sup>7</sup>

In this paper, we present results concerning the vibrational relaxation and electronic state transfer for the XeCl(B,C) states in various bath gases. We chose XeCl because of the ease of obtaining experimental data and because assignment of vibrational distributions from the bound-free spectra is more straightforward. The general findings from the XeCl results, should be extendable to other RgX systems. We discuss in detail the results for XeCl\* in argon and subsequently contrast the relaxation processes in Ar with those in He, Ne, Kr, Xe and N<sub>2</sub>. The final results are in the form of state-to-state rate constants for C-B transfer and for vibrational relaxation as a function of vibrational level. In addition to applications to rare gas halide lasers, the results are of general

interest for relaxation of high vibrational levels of ionic diatomic molecules in rare gases.

Reactive quenching of  $\text{Xe}({}^3\text{P}_{2,1})$  with halogen donors gives  $\text{XeCl(B,C)}$  with various vibrational distributions and using different donors permits a range of the vibrational levels to be emphasized. For instance, the donors  $\text{Cl}_2$ ,  $\text{CCl}_4$  and  $\text{COCl}_2$  give vibrational distribution peaking at  $v=0$ , 50 and 100, respectively.<sup>5b</sup> Computer simulation of the B-X and C-A emission spectra permits assignment of the vibrational distribution. Initial distributions are obtained from low pressure ( $<0.2$  torr) spectra where collisions with the bath gas are not important. At higher pressures the appearance of the B-X and C-A emissions, as well as their relative intensities, change as a consequence of vibrational relaxation and transfer between the two electronic states by bath gas collisions. By modeling the population distributions and the B/C intensity ratios as a function of bath gas pressure, rate constants for relaxation and transfer can be deduced, as well as a state-to-state view of these processes. The state-to-state kinetics are emphasized in this paper; however, the results are of practical relevance because the rare gas halide formation processes in lasers, whether they be reactive quenching of excited rare gas atoms or ion-ion combination, initially yield high vibrational levels of  $\text{RgX(B,C)}$ .

The organization of the paper is as follows. In section II the experimental results for the reactions of  $\text{Xe}({}^3\text{P}_{2,1})$  with  $\text{Cl}_2$ ,  $\text{CCl}_4$ , and  $\text{COCl}_2$  in various bath gases are summarized. Also the  $\text{XeCl(B,C)}$  vibrational distributions obtained from simulation of spectra are presented. The  $\text{XeCl(B-X)}$  and  $\text{XeCl(C-A)}$  simulation is nearly the same as used previously<sup>5b</sup> and this is only briefly mentioned. Section III gives the details of the modeling procedures used to reproduce the variation of the populations with pressure. The detailed results for Ar are given in Section IV and a summary of the other gases is given in Section V. A discussion is given in Section VI.

## II. EXPERIMENTAL RESULTS AND SPECTRAL SIMULATIONS.

The experimental details for study of the  $\text{Xe}({}^3\text{P}_2)$  and  $\text{Xe}({}^3\text{P}_1)$  atom reaction with chlorine donors have been given elsewhere<sup>3,7</sup> and can be briefly summarized here. The metastable atom reactions are studied with a flowing afterglow apparatus. A small amount of Xe is entrained in an Ar carrier gas flow which is passed through a low power hollow cathode discharge.  $\text{Xe}({}^3\text{P}_2)$  is formed from direct excitation in the discharge and from excitation transfer from  $\text{Ar}({}^3\text{P}_2) + \text{Xe}$ . Only the relatively long lived  $\text{Xe}({}^3\text{P}_2)$  survives the transit time to the reaction zone several cm. downstream of the discharge. The chlorine donor is added coaxially to the Ar/Xe flow in the reaction zone and the resulting  $\text{XeCl}^*$  emission is observed with a monochromator and detection system interfaced to a minicomputer. The computer controls data acquisition and stores the spectra on magnetic tape for subsequent analysis.<sup>8</sup> The spectra can be corrected for the spectral response of the detection system, integrated to obtain (B-X) and (C-A) emission intensities, and replotted for direct comparison with simulated spectra. The pressure at which the spectra are observed can be changed by varying the Ar flow and/or throttling the pumping speed. The flowing afterglow method is somewhat limited in that only inexpensive gases (Ar) can be routinely used as the carrier gas and the pressure range is restricted from 0.2 to  $\sim 50$  torr.

For the resonance state atom reactions a mixture of Xe, chlorine donor, and bath gas, under either static or flowing conditions is irradiated in a reaction cell, with a microwave powered Xe resonance lamp interfaced to the cell with a  $\text{MgF}_2$  window. Radiation trapping in the cell lengthens the effective lifetime of  $\text{Xe}({}^3\text{P}_1)$  to a time scale permitting reaction to occur. The  $\text{XeCl}^*$  emission is observed, at right angles to the light from the resonance lamp, with the same detection system as above. Relative to the flowing afterglow, this method has the advantage of a much larger pressure range, 0.1 torr to 5 atm, as well as permitting different bath gases to be used. One disadvantage is scattered light, mainly  $\text{Xe}^*$  lines, from the discharge which overlap the long wavelength part of the

XeCl(C-A) spectrum. The intensity of the atomic lines must be carefully subtracted out to obtain accurate B/C intensity ratios. In all of the work here the small (the calculated B-A/B-X branching ratio is 0.06) contribution of the B-A transition to the C-A spectrum has been ignored.

Sample XeCl spectra obtained with the above methods are shown in Figs. 1-3 for various donors and pressures of argon. Although close examination does show slight differences resulting from the  $978 \text{ cm}^{-1}$  higher energy for the resonance state, the spectra from the  $\text{Xe}(^3\text{P}_1)$  and  $\text{Xe}(^3\text{P}_2)$  reactions are virtually identical and in the remainder of this paper no distinction will be made between them. Plots of the intensity ratio,  $I_B/I_C$ , vs pressure are shown in Fig. 4a-b for the reactions of  $\text{Xe}^* + \text{Cl}_2$ ,  $\text{CCl}_4$  and  $\text{COCl}_2$  in argon and for  $\text{Xe}^* + \text{Cl}_2$  in various bath gases.

The numerical simulation of the experimental bound-free spectra has been presented elsewhere.<sup>5</sup> Three basic variables enter into the simulations; relative shapes of the two potentials, variation of the transition moment with inter-nuclear distance and the vibrational distributions. The variation of the transition moment is especially important in fitting the bound-free emission. In this work, we used the procedure developed previously for fitting the XeCl(B-X) emission, which employed Tellinghusin's B state potential in a Rittner form with a flat potential for the X state.<sup>5b</sup> The effects of the transition moment was included by introducing a monotonic function to multiply the spectrum obtained using a constant transition moment. These results were successful in simulating the XeCl(B-X) emission from a variety of donors. The B-X transition is easy to simulate because the spectra are not very sensitive to the shape of the lower potential; such is not the case for the C-A transition where the repulsive wall for the lower state A-potential is very important. Initially we used the potentials previously employed to simulate the C-A transition. However, when modeling the XeCl(B) distribution as a function of pressure, a second maximum developed in the distribution from C→B collisional transfer. This second peak, which is not experimentally observed, was a consequence of the initial C distribution having its maximum at lower  $E_\gamma$  than for XeCl(B). This is evident in Figs. 4 and 7

of ref 5b where  $E_{mp}$ (XeCl,B) is 6 kcal mole<sup>-1</sup> larger than  $E_{mp}$ (XeCl,C) from the Xe\* + Cl<sub>2</sub> reaction. To rectify the problem it was necessary to make the A state slightly more repulsive so that the vibrational distribution from the C-A emission was moved to higher  $E_V$ . The initial XeCl(C) distributions used here from Cl<sub>2</sub>, CCl<sub>4</sub> and COCl<sub>2</sub> were indistinguishable from the XeCl(B) distributions.

The expressions for the potentials used here to simulate the C-A emission are

$$V(R)^{C,3/2} = \frac{\omega_e^{C,3/2}}{\omega_e^{B,1/2}} V^T(R')_{B,1/2} \text{ cm}^{-1} \quad a)$$

$$V(R)^{A,3/2} = 1.77 \times 10^7 \exp(-2.827 R') \text{ cm}^{-1} \quad b)$$

where  $V^T(R')_{B,1/2}$  is given by eqn 4a of ref. 5b,  $R' = R_e^{B,1/2} + 0.9814(R-R_e^{C,3/2}) - 0.0365(R-R_e^{C,3/2})^2$ ,  $\omega_e^{B,1/2} = 195.2 \text{ cm}^{-1}$ ,  $\omega_e^{C,3/2} = 188 \text{ cm}^{-1}$ ,  $R_e^{B,1/2} = 2.937 \text{ \AA}$ , and  $R_e^{C,3/2} = 3.14 \text{ \AA}$ . It should be noted that the expressions for the A potential and the transition moment function of ref. 5b (eqn 14 and 15) are slightly in error.<sup>9</sup>

The basic procedure for simulating the experimental spectra is to first calculate spectra for individual vibrational levels of the upper state. These individual spectra are then summed over an assumed vibrational distribution to obtain a total spectrum. Different vibrational distributions were tried until a satisfactory fit was found for the experimental spectra obtained at different pressures. Some simulated spectra are compared to the experimental ones in Figs. 1-3 and the corresponding steady-state vibrational distributions are shown in Fig. 5-7.

Two important points affecting the modeling are the reliability of the distributions, i.e. how accurate are the simulations, and the variation of the XeCl\* lifetime with v level. The first point is addressed in Fig. 8, which shows XeCl\*(B-X)emission spectra in Ar from Xe\* + Cl<sub>2</sub> at 1.3 torr and from Xe\* + CCl<sub>4</sub> at 11.9 torr along with two simulated spectra that were judged to be satisfactory fits. The corresponding vibrational distributions differ

by  $\sim$  10% on the average. Hence, any relaxation model that matches a distribution to within  $\sim$  10% of the distribution assigned by simulation must be considered satisfactory. The uncertainty in the distributions increases with increasing pressure (reduction in vibrational energy) because of the loss of the oscillations from the spectra. This is evidenced by the spectrum from  $\text{CCl}_4$  for which the distributions are less unique than for the low pressure  $\text{Cl}_2$  spectra. Above  $\sim$  15 torr of Ar, the oscillations have disappeared and the best that can be done is to assign high temperature Boltzmann distributions. The above discussion was based on the B-X spectrum. For the C-A spectra, the potential curves are less accurate and the B-A and C-A emission overlap; therefore, the distributions from the spectral simulations are less reliable than those from the B-X simulations. Hence in modeling, emphases was placed on fitting first the  $I_B/I_C$  ratio vs pressure, the B state vibrational distribution, and finally the C state vibrational distribution.

The second point was the variation of the  $\text{XeCl}(B,C)$  lifetimes with  $v$  level. Unfortunately measurements of the  $\text{XeCl}(B,C)$  lifetimes have not been reported. However, the theoretical values given by Dunning and Hay<sup>10a</sup> for  $\text{XeCl}(B,v=0)$ , 11 nsec, and  $\text{XeCl}(C,v=0)$ , 120 nsec, can be combined with the dependence of the transition moment on internuclear distance to obtain calculated lifetimes. The Einstein coefficients decrease by  $\sim$  3 from  $v=0$  to 100; therefore, the lifetimes increase by  $\sim$  3. This trend of increasing lifetime vs.  $v$  level has been observed for a small range of  $v$  for  $\text{KrCl}$ .<sup>11</sup> Dunning and Hay have calculated lifetimes for  $\text{ArF}$ ,  $\text{KrF}$  and all the xenon halides.<sup>10</sup> Experimental lifetimes have been reported for  $\text{KrF}(B)$ <sup>12a</sup> and  $\text{XeF}(B,C)$ <sup>12b</sup>; the results tend to agree with the calculated values to within  $\sim$  30%. The  $\text{XeCl}$  calculated lifetimes and energy levels used in the modeling calculations are summarized in Table 1.

Even without the modeling results, some general conclusions can be drawn from the data.<sup>13,7</sup> The statements below refer to argon bath gas but the same trends are

observed in other bath gases; but, the characteristic pressure regions are different. At zero pressure, the initial  $I_B/I_C$  is 1.3 to 1.5 for all 3 donors,  $\text{Cl}_2$ ,  $\text{CCl}_4$ ,  $\text{COCl}_2$ . In the low pressure ( $\leq 5$  torr) regime, B state vibrational relaxation, C state vibrational relaxation, and a rapidly increasing  $I_B/I_C$  is observed. Since at these pressures, the lifetime of the B state is less than the time between collisions with bath gas, the apparent B state relaxation is due to collisional transfer from the C state. This is also the cause of the increasing  $I_B/I_C$  ratio. A simple steady state analysis for  $\text{XeCl}(\text{B})$  and  $\text{XeCl}(\text{C})$  similar to those used previously<sup>4a,7</sup> can be used to obtain approximate rate constants for C to B transfer,  $k_{CB}$ , from the variations of  $I_B/I_C$  vs pressure in the low pressure regime. The analysis, which included an average radiative lifetime estimate for each electronic state gave  $k_{CB}$  of 18, 17, 5.9, and  $2.7 \times 10^{-11} \text{ cm}^3 \text{ molec}^{-1} \text{ sec}^{-1}$  for Kr, Ar, Ne, and He, respectively. Since the reaction of  $\text{Cl}_2$  with  $\text{Xe}^*$  gives a high vibrational distribution, these rate constants refer to  $v \approx 100$ . The  $I_B/I_C$  ratios from  $\text{CCl}_4$  and  $\text{COCl}_2$  do not increase as fast as for  $\text{Cl}_2$ ; hence, the transfer rate constants evidently are smaller for lower v levels. This is supported by the fact that the change in  $I_B/I_C$  "slows down" for higher pressure and in the intermediate regime (5 to 50 torr of Ar)  $I_B/I_C$  is nearly constant. In this regime collisions with the B state become important and the slow change of  $I_B/I_C$  is due a combination of reduced transfer rate constants for the lower v levels and also to the balance in B and C state populations as the B-C transfer rate competes with radiative decay of the B state. At  $\sim 50$  torr the  $I_B/I_C$  attains its maximum value. Examination of the 10-100 torr spectra indicates that the vibrational distributions are high temperature Boltzmann distributions, while the electronic state distribution is non-Boltzmann. By  $\sim 100$  torr, the vibrational distributions are nearly 300K. As the pressure is increased to the 1000 Torr region, the  $I_B/I_C$  ratio decreases as transfer between B and C occurs to give a Boltzmann electronic state distribution. At the highest pressures electronic transfer is complete and interpreting the high

pressure  $I_B/I_C$  ratio as a 300K distribution shows that the XeCl(C) state is  $\sim 200 \text{ cm}^{-1}$  lower in energy than the XeCl(B) state.<sup>7</sup> The exact value of the energy separation is still being discussed. Tellinghusien and McKeever<sup>14a</sup> report a value of  $\sim 130 \text{ cm}^{-1}$  by interpreting the  $I_B/I_C$  high pressure intercept at 360K and 800K. (In addition they were able to obtain  $\frac{A_{C-A}}{A_{B-X}} \approx \tau_B/\tau_C$  of 0.087 which is excellent agreement with the calculated value of 0.091). Bokor and Rhodes<sup>14b</sup>, on the other hand, report an energy separation of  $\sim 5\pm 25 \text{ cm}^{-1}$  with the C state higher in energy. However, their experiments, which used an ArF laser to excite Xe/Cl<sub>2</sub> mixtures in Ar, extend to only 1000 torr. In fact pressures of  $\gtrsim 1000$  torr are required to obtain B/C equilibrium concentrations (see Fig. 2 of ref. 7 for example). Thus, the data of Bokor and Rhodes do not extend to sufficiently high enough pressure to obtain a true equilibrium  $I_B/I_C$  ratio. Experiments of the type described in ref. 7 have recently been performed at low temperatures<sup>15</sup> and preliminary results support an energy separation of  $\approx 200 \text{ cm}^{-1}$ . The uncertainty of the B-C energy separation does not affect interpretations of this paper because we are concerned with collisions of XeCl molecules in high v levels.

### III. METHODS FOR MODELING VIBRATIONAL RELAXATION AND B-C STATE TRANSFER

The method used to model the variation of the XeCl(B,C) vibrational distributions and B/C ratio as a function of pressure is essentially the same as the one used by Duewer, et al<sup>16</sup> in studying the rotational relaxation of CN(B,v=11). The one important difference here is the large variation in radiative lifetime which must be included in the calculation. Electronic quenching of XeCl(C,B) is assumed to be unimportant since the modeling only extends to 50 torr. The vibrational levels of XeCl(B,C) are divided into three ranges: low v (v=0-30), mid v (v=30-70), and high v (v=70-130). Examination of Figs. 5-7 shows that Xe\* + Cl<sub>2</sub> gives an initial vibrational distribution

peaked at  $v \sim 100$  with  $\geq 80\%$  of the total in the high  $v$  range;  $Xe^* + CCl_4$  gives an initial distribution peaked at  $v \sim 50$  with 80% in the mid  $v$  range, and  $COCl_2$  gives a distribution marked at  $v=0$  with 80% in the low  $v$  range.

If the relative populations of  $XeCl(B,v)$  and  $XeCl(C,v)$  are considered to be a vector, then the normalized initial population vector,  $X(0)$ , is given by

$$X(0) = R_i / \sum R_i \quad (2)$$

where  $R_i$  is the formation rate into the  $i$ th level. If  $N_C$  and  $N_B$  are the maximum number of vibrational levels for  $XeCl(C)$  and  $XeCl(B)$ , respectively, the total C and B populations are

$$N_C = \sum_{i=1}^{NC} X_i(0) \text{ and } N_B = \frac{\sum_{i=1}^{NC+N_B} X_i(0)}{NC}. \quad (3)$$

Since the reaction of  $Xe^* + Cl_2$  populates levels up to  $v=140$  in the C state,  $X(0)$  would include over 200 levels if each vibrational level was included.

To save computational time, the populations were grouped into every 4th vibrational level. The relative B to C formation rate is given by<sup>4b</sup> the zero pressure  $I_B/I_C$  ratio, which was taken as 1.4 for all three donors from Fig. 4. The initial relative vibrational distribution within each electronic state was obtained from the simulation of the lowest pressure, typically  $\leq 0.2$  torr, spectrum. The low pressure distributions shown in Fig. 5-7 are steady-state distributions and must be corrected for the lifetime variation to obtain the true initial distributions.<sup>5b</sup>

The relative populations that exist after exactly  $m$  collisions are given by

$$X(m) = \tilde{P}^m X(0) \quad (4)$$

The transition matrix  $\tilde{P}$ , has elements,  $P_{ij}$ , which give the probability per collision with bath gas of a  $XeCl$  molecule in state  $j$  going to state  $i$ .  $\tilde{P}$  was partitioned into 4 parts as follows:

for $1 \leq i \leq NC$	$1 \leq j \leq NC$	$P_{ij}^R = C$ state relaxation
for $1 \leq i \leq NC$	$1 \leq j \leq NC + NB$	$P_{ij}^T = B$ to $C$ transfer
for $NC+1 \leq i \leq NC+NB$	$1 \leq j \leq NC$	$P_{ij}^T = C$ to $B$ transfer
for $NC+1 \leq i \leq NC+NB$	$NC+1 \leq j \leq NC+NB$	$P_{ij}^R = B$ state relaxation

The diagonal elements of the matrix correspond to elastic collisions, which are unobservable in this case, and were calculated from the normalization condition.

$$P_{ji} = 1 - \sum_i P_{ij} \quad i \neq j \quad (6)$$

By normalizing  $\tilde{P}$  in this manner, the sum of the inelastic and elastic rate processes is independent of vibrational level providing the collision frequency (cross-section) is selected to be constant for all levels. In the modeling the collision frequency was taken as a constant; but, the ratio of the inelastic and elastic cross-sections was allowed to be a function of vibrational level. The transition matrix is subject to detailed balance and up transitions were calculated from the model assumed for the down transitions, i.e. for  $j > i$ .

$$P_{ji} = P_{ij} e^{-(E_j - E_i)/kT} \quad (7)$$

The probability that a molecule undergoes exactly  $m$  collisions before decaying by photon emission can be calculated as follows. For a molecule in a given level with a radiative lifetime,  $\tau$ , the distribution of times for radiative decay is given by

$$F(t) = \tau^{-1} e^{-t/\tau} \quad (8)$$

The fraction of molecules undergoing exactly  $m$  collisions in a fixed time interval  $t$  is given by

$$F(m) = \frac{(zt)^m}{m!} e^{-zt} \quad (9)$$

where  $z$  is the collision rate corresponding to a given pressure. The distribution for the number of collisions before radiative decay is given by the convolution of these two distributions over all time,

$$A(m) = \int_0^{\infty} \tau^{-1} e^{t/\tau} \left(\frac{zt}{m!}\right)^m e^{-zt} dt \\ = \frac{\tau^{-1}}{z+\tau-1} \left(\frac{m}{z+\tau-1}\right)^m$$
(10)

This last quantity is the fraction of molecules undergoing emission after exactly  $m$  collisions but before the  $m+1^{\text{th}}$  collision. The emission intensity,  $I$ , from each level in the form of a vector is given by,

$$I = \sum_{m=0}^{\infty} A(m) X(m) \\ = \sum_{m=0}^{\infty} A(m) P^m X(0),$$
(11)

where  $A(m)$  is a vector and is different for each level because of the different values of  $\tau_i$ . Although this equation contains an infinite number of terms, the summation can be approximated with a finite number of terms,  $m^*$ , because  $A(m)$  decreases with increasing  $m$ . In this work the summation was terminated when  $\sum_i X_i(m^*)$  was  $\leq 0.1\%$  of  $X_i(0)$ . For this criteria  $m^*$  usually ranged from 2 to 100 depending on pressure and bath gas. The intensity from individual levels is summed to obtain the  $I_B/I_C$  ratio. The intensities were converted to steady-state concentrations,  $X_i(s)$ , by

$$X_i(s) = I_i \tau_i.$$
(12)

If lifetimes for all levels were equal, the relative steady-state concentrations and intensities would be equivalent and no conversion would be needed. The distributions given by  $X_i(s)$  are compared to the distributions obtained from simulation of the experimental spectra at a given pressure to gain information about the form of  $P_{ij}$ .

Assignment of the model for  $P$  was based on a trial and error approach. We began with simple models and added more flexibility as necessary. We wanted overall rate constants for transfer and vibrational relaxation, as well as state-to-state rate constants. The state-to-state processes are determined by the

form of  $\tilde{P}$  and the rate constants by  $z \sum_i P_{ij}$  ( $i \neq j$ ). The success of a model for  $P$  is judged by how well the calculated distributions fit the variation of the shape of the simulated distributions with change in pressure. On the other hand, the rate of relaxation of the vibrational distributions as a function of pressure depends on both the collision rate  $z$  (or  $\sigma$ , the total collision cross-section) and  $\tilde{P}$ . For our purposes the only restriction for  $\sigma$  is that it be large enough to give the required rates of relaxation and transfer. Initially, we estimated "reasonable" values for the collision cross-section and proceeded with the modeling. But in some cases it was subsequently necessary to increase  $\sigma$  because the required rates of relaxation and transfer could not be made fast enough for the first choice for  $\sigma$ . After selection of a  $\tilde{P}$  that fitted the overall shape of the distributions, though not necessarily at the right pressures, the inelastic cross-section could be increased or decreased until the distributions matched at the proper pressure.

The objective is to obtain a model for the transition matrix,  $\tilde{P}$ , which simultaneously fits all of the experimental data; i.e. the B and C distributions and the  $I_B/I_C$  ratio as a function of pressure for all three Cl donors. Preferably the model should be described by as few independent parameters as possible. Calculations first were done for XeCl in Ar. Relaxation and transfer are both sufficiently fast that changes occur at relatively low pressure. Since the required number of iterations needed for convergence depends on pressure, analysis of the argon data for a given degree of relaxation, requires less computer time than for He or Ne. The fitting for Ar also provides a good reference point for both lighter and heavier bath gases. To aid in the discussion and in identification of results, each model will be given a label (capital letter) as it is presented. Several different models were tried. Each of these models has several parameters which can be varied, but we present only the best set of parameters from the several trial and error attempts to obtain a satisfactory fit to the experimental data. Table 2 contains a summary of the models and the collision cross-sections.

#### IV. RELAXATION IN ARGON

##### IV A. Vibrational Relaxation of XeCl(C, high v), Model A.

The XeCl(B) radiative lifetime is less than the time between collisions for pressures  $\leq$  2 torr and, B to C transfer can not be important. Therefore, the change in the XeCl(C) distribution is solely due to vibrational relaxation. Although this statement is qualitatively correct, 20% of the XeCl(B, v=100) molecules undergo at least one collision at 0.5 torr. This percentage increases to 40% at 1 torr and  $\sim$  55% at 2 torr; but, as a first approximation, B to C transfer can be ignored and C state relaxation can be modeled as vibrational relaxation for pressures  $\leq$  2 torr.

The initial model used to calculate the transition matrix elements,  $P_{ij}^R$ , for transitions  $j > i$  was given by

$$P_{ij}^R = \frac{akT}{\Delta E} + \exp(-\frac{b\Delta E}{kT}) \quad (13)$$

with  $\Delta E = E_j - E_i$ . The constants a and b were treated as adjustable parameters and were varied to obtain a satisfactory fit to the data. The kT factor ( $k =$  Boltzmann constant and  $T = 300^\circ K$ ) serves to make  $\Delta E$  unitless and has no other physical significance. For some values of a and b,  $\sum_{i \neq j} P_{ij}^R$  was greater than 1 and values of  $P_{ij}^R$  calculated by the above equation were multiplied by a normalization constant so that  $\sum_i P_{ij}^R = 1$ . Certain variations of the above model also were explored;  $P_{ij}^R = a + \exp(-b\Delta E/kT)$ ,  $P_{ij}^R = akT/\Delta E$ , and  $P_{ij}^R = \exp(-b\Delta E/kT)$ , and close fits were obtained for most of these variations. However, the "best" overall fit was obtained with eqn. 13 for  $a = 1.0$  and  $b = 0.11$ . With normalization the best model for  $\hat{P}$  was

$$P_{ij}^R = \frac{1}{20} \left( \frac{kT}{\Delta E} + \exp(-0.11 \Delta E/kT) \right), \quad (14)$$

which will be referred to as Model A, with a collision diameter of  $4.95 \text{ \AA}^\circ$ . The dominant contribution to the magnitude of  $P_{ij}^R$  is given by the exponential term and

since the vibrational relaxation could be fit satisfactorily with just an exponential term, the other models presented later do not include the  $kT/\Delta E$  term.

The population distributions resulting from model A are compared in Fig. 9 to the simulated distributions at several pressures. The fit is well within the 10% uncertainty of the experimental distributions throughout the 0.11 to 2.2 torr range. Note especially the good fit for  $P = 2.2$  torr for  $20 \leq v \leq 110$ . By combining the collision frequency and the  $\sum_i P_{ij}$  values the relaxation rate constants,  $k_R (10^{-11} \text{ cm}^3 \text{ molec}^{-1} \text{ sec}^{-1})$  as a function of  $v$  level are 4.5 - 13, 13 - 20, and 20 - 34 for  $v = 4-30$ , 30-70, and 70-130, respectively. The smooth increase of the rate constants with  $v$  is due to the smaller energy separation between high  $v$  levels and the larger number of levels below a given  $v$  level.

For model A the  $P_{ij}^R$  decline smoothly with increasing  $\Delta E$ . Single quantum jumps, (which for our model includes all transitions from  $v$  to  $v-1$ ,  $v-2$ ,  $v-3$ , and  $v-4$ ) are the most important; however, multiquantum transitions also are significant. The adjustable parameter  $b$  in the exponential term governs the range of  $\Delta E$ . For small  $b$ , the low  $v$  range gains in population at the expense of the high  $v$  and the distribution is broadened, whereas for larger  $b$  the distribution remains sharp and moves systematically to lower  $v$ . For a successful fit  $b$  must be 0.1 - 0.2. The success of this model is due to the fact that molecules in the high  $v$  range ( $v = 70 - 130$ ) have a significant probability of transfer to the low  $v$  range ( $v = 4 - 30$ ). This must be a general feature of all models that fit the relaxation of XeCl(high  $v$ ) in Ar.

Since the distribution from  $\text{Xe}^* + \text{Cl}_2$  is in the high  $v$  range, the model should be most reliable for these levels. Most of the population in the low  $v$  levels from  $\text{Xe}^* + \text{Cl}_2$  arises from multiple collisions and the model may not be too reliable for the transition probabilities of the lower levels.

#### IV-B. Vibrational Relaxation and Transfer of XeCl (high v) - Model B

Before proceeding with the addition of the XeCl(B) state to the calculations, certain assumptions must be made. Because C to B transfer is an important process at low pressure, apparent vibrational relaxation of B is observed before bath gas collisions with B are important. At higher pressures where XeCl(B) + bath gas collisions become important, the vibrational distribution of XeCl(B) has relaxed so much that obtaining information about XeCl(B) vibrational relaxation is impossible. Without any knowledge to the contrary, we will assume that B state relaxation can be described by the same model as for XeCl(C). We will drop the  $kT/\Delta E$  term because of its minor role, and the model for vibrational relaxation becomes

$$P_{ij}^R = \exp(-b\Delta E/kT). \quad (15)$$

Since the vibrational levels of (C) are closer together than for (B), the  $k_R^R$ (B) are slightly smaller, typically by 10-20%, than  $k_R^R$ (C) for the same v level.

The additional assumption concerns B  $\rightarrow$  C transfer. For the same reasons as given above, reliable information for B-C transfer from XeCl(B, high v) is not available. However, detailed balance can be used to relate the forward and reverse B-C transfer rates. At limiting high temperature the populations of both states would be equal and  $k_{BC} = k_{CB}$ . Although the translational temperature is near 300K, it is reasonable to assume that for high vibrational excitation  $k_{BC}(v) \approx k_{CB}(v)$  and that the form for  $P_{ij}^T$  is the same for both XeCl(B) and XeCl(C). The XeCl(C,v=0) level, which represents the total v=0-3 population) is the lowest level and has no down transition, hence, its  $k_T$  and  $P_{ij}$  values are determined completely from detailed balance. The coarse graining will result in an increasing erroneous representation as the XeCl population builds up in the lowest levels of B and C.

In contrast to modeling the C state vibrational relaxation, simultaneous fitting of the B and C distributions and the  $I_B/I_C$  ratio as a function of pressure was extremely difficult. Considerable effort was expended in obtaining a model that was sufficiently flexible. We initially used the same form for  $P_{ij}^T$  that was used for vibrational relaxation and varied the parameters, as well as the relative importance of transfer vs. relaxation. For a given C level the highest transfer probability will be to the adjacent lower B level, according to this model. For certain values of the parameters, the  $I_B/I_C$  ratio could be matched (and also C state vibrational relaxation), but the B state vibrational distribution was always too high in energy. An additional problem arises because the energy difference between adjacent B and C levels (note, our calculation uses every fourth real level) is not constant with  $v$ , because the values of  $\omega_e$  and  $\omega_e x_e$  for XeCl(B) and XeCl(C) differ and the calculation gave  $P_{ij}^T$  of widely varying magnitude for adjacent levels, which led to spikes in the B distribution which were difficult to compare with the smooth simulated distributions. Improvements were necessary to rectify these problems.

The final model adopted for  $P_{ij}^T$  requires that the most probable transition from a given J be to the energy region  $E_o$  and has the following form

$$P_{ij}^T = \frac{kT}{C} \int_{E_i}^{E_{i+1}} \exp(-C \cdot E^*/kT) dE^* \quad E^* = |\Delta E - E_o| \quad (16)$$

where  $kT$  and  $\Delta E$  are defined as before and  $C$  is the adjustable parameter and  $E_o$  is given by

$$E_o = (1.0 - f^* E'_j) E_j \text{ cm}^{-1} \quad (17)$$

where  $E'_j = E_j/16000 \text{ cm}^{-1}$  ( $16000 \text{ cm}^{-1}$  is approximately the energy of the highest populated levels in the  $\text{Xe} + \text{Cl}_2$  reaction) and  $f$  is an adjustable parameter.

Eqn. 16 allows the most probable transfer to be fixed at  $E_o$ , with  $E_o$  being some fraction of initial energy. With the benefit of hindsight the  $E_j/16000 \text{ cm}^{-1}$  term was added so that the lower  $v$  levels would lose less energy than higher  $v$  levels. The use of the integral in eq. 16 eliminates the computational artifact

of widely varying  $P_{ij}^T$  for adjacent levels and gives smooth steady-state B distributions. However the integral also gave nearly constant  $\sum_i P_{ij}^T$  values, which are independent of  $j$ , and hence, the  $k_T$  are independent of vibrational level. To regain the ability to control the magnitudes of  $k_T$  for different  $v$  levels the  $\sum_i P_{ij}^T$  values were fixed by a series expansion

$$\sum_{i < j} P_{ij}^T = T_1(T_2 + T_3 E_j' + T_4 E_j'^2) \quad (18)$$

where  $T_i$  are adjustable parameters. To increase flexibility, a similar expression was used for  $\sum_i P_{ij}^R$

$$\sum_{i < j} P_{ij}^R = R_1(R_2 + R_3 E_j' + R_4 E_j'^2) \quad (19)$$

with  $R_i$  adjustable. The factors  $R_1$  and  $T_1$  allow the magnitude of  $k_T$  and  $k_R$  to be altered by changing the ratio of elastic and inelastic components of the cross section. The parameters  $R_2-R_4$  and  $T_2-T_4$  provide the functional dependence of  $\sum_i P_{ij}$  on  $v$  level. The most extensive experimental data exists for Ar as the bath gas. For this reason  $R_2-R_4$  and  $T_2-T_4$  were established for Ar and were not changed for the other bath gases. Several calculations were done to determine a good set of parameters. Model B was chosen as giving the best fit to the  $Xe^* + Cl_2$  data. The parameters for Model B are  $b = c = 0.1$ ,  $f = 0.15$  and  $T_i = 1.2, 0.01, 0.7, -0.5$ ,  $R_i = 0.1, 0.01, 1.0, -0.3$  for  $i = 1, 2, 3, 4$ , respectively. The calculated results are compared to the experimental distributions and  $I_B/I_C$  ratios in Fig. 10-11. The fit is fairly good for the B-state distribution. The fit to the C-state distributions, while not as good as for Model A, is still within the uncertainty of the distributions. The  $I_B/I_C$  fit is excellent below  $\approx 5$  torr and is only slightly low for the higher pressures. In fact, the calculated  $I_B/I_C$  ratio begins to decrease at 8 torr while the experimental points continue to rise. This suggests that the transfer rate constants for the lower  $v$  levels are too low relative to the high  $v$  levels and/or that the C-state is vibrationally relaxing too fast. In either case, as the C-state

population builds up in low levels, the C to B transfer slows down with increasing pressure. The second reason is substantiated by the 8.0 torr results of Fig. 10, which shows that the calculated populations are too high in the low  $v$  range where the C-B transfer rate constants are the smallest. Since the calculations match lower pressure data where the distribution is largely above  $v=70$ , this model was considered successful in fitting the  $\text{Xe}^* + \text{Cl}_2$  data. In the next section Model B is modified slightly to give a good fit to the  $\text{Xe}^* + \text{CCl}_4$  data with a distribution that initially is in the mid  $v$  range and the question concerning the relaxation and transfer rates for  $v=30-70$  will be addressed then.

Combination of the transition probability matrix elements with the collision frequency gives the rate constants listed in Table 2. The relaxation rate constants agree favorably with the results from Model A. The  $k_R$  calculated here are slightly larger than for Model A and as discussed above, may be too large for the low and mid  $v$  range. Nevertheless, the good fit to the data suggest that the  $k_R$  for the high  $v$  range are  $20-35 \text{ } 10^{-11} \text{ cm}^3 \text{ molec}^{-1} \text{ sec}^{-1}$ . The good fit to the B state distribution and the  $I_B/I_C$  ratio below 5 torr suggests that the  $k_T$  are also reliable, at least for high  $v$  levels. The form of  $P_{ij}^R$  was discussed when Model A was presented and the results for Model B are very similar (see Figure 13); however, the form of  $P_{ij}^T$  differs from  $P_{ij}^R$ . The C molecules enter the B state in an energy range that is peaked at  $\sim 10-15\%$  below the initial energy level.

#### IV-C. Relaxation and Transfer of $\text{XeCl}(\text{mid } v)$ and $\text{XeCl}(\text{low } v)$ - Model C

Since a satisfactory fit was provided to the  $\text{Xe}^* + \text{Cl}_2$  data, model B was used to examine the data from the  $\text{Xe}^* + \text{CCl}_4$  reaction, which emphasizes the mid- $v$  range. The results are shown in Fig. 12 for three pressures and, as can be seen, the B and C states both relax too fast and  $I_B/I_C$  increases too slowly

with increasing pressure (Fig. 11). The following improvements are needed. Since  $\text{XeCl}(\text{C})$  relaxes too fast,  $k_R(v=30-70)$  should be reduced. The low  $I_B/I_C$  could be a consequence of the (too) fast relaxation of the C state and/or  $k_T$  being too small for  $v=30-70$ . Since the B state also relaxes too quickly,  $k_T$  probably is too large or transfer occurs with too large a loss of energy. The most probable energy loss by transfer of molecules from  $\text{C}(v=50)$  to  $\text{B}(v)$  is only 7-8% of the initial energy and further reduction of this will not give much improvement. Hence, the best way to simultaneously reduce the rate of B-state relaxation and increase the  $I_B/I_C$  ratio is to increase the C parameter in eqn. 16; this gives a sharper v-level distribution entering the B state. In addition decreasing  $k_R$  to fit the C relaxation will increase  $I_B/I_C$ . The following modifications to Model B were made:  $R_1$  was changed to 0.50 which reduced  $k_R$  by a factor of  $\sim 2$ ; the parameter C in eqn. 16 was changed to 0.2 which reduced the B state relaxation rate, and b was increased to 0.15, which gave a slightly better fit than using  $b=0.10$ . The rest of the parameters were the same as for Model B. The results from this calculation, hereafter denoted as Model C, are compared in Figs. 11 and 12 and the fit is seen to be much improved. The calculated transfer rate constants for Model C are the same as for Model B and the only difference is the form of  $P_{ij}^T$ . The relaxation rate constants for Model C are 1.0-6.0 and 6.0-12  $10^{-11} \text{ cm}^3 \text{ molec}^{-1} \text{ sec}^{-1}$  for the low v and mid v range, respectively. The results for low v are less reliable than for mid v because low v levels are populated by multiple collisions. The Model C rate constants, which are approximately half the values from Model B, should be more reliable because i) the fit to the  $\text{CCl}_4$  results are better and ii) the effect of multiple collisions is less severe in the mid and low v range for the  $\text{CCl}_4$  data than for the  $\text{Cl}_2$  data.

Model C was used to examine the  $\text{Xe}^* + \text{COCl}_2$  data. The fit to the  $I_B/I_C$  data shown in Fig. 11, though not as good as for the other two reactions, is satisfactory. The distributions based on simulation of the  $\text{Xe}^* + \text{COCl}_2$  spectra are

only qualitatively reliable because lack of oscillatory structure in the spectra prevents reliable assignment of the vibrational distributions. Nevertheless, Model C does give acceptable results and no attempt was made to further improve the model for the low  $v$  regime.

## V. RELAXATION AND TRANSFER IN OTHER BATH GASES

### V-A. XeCl(high $v$ ) in Helium and Neon

In this section we extend the model to include other bath gases. For the most part these results are based on the  $\text{Xe}^* + \text{Cl}_2$  reaction and will be strictly valid only for XeCl high  $v$ . Only the final results will be stated. Examples of the results of the simulation and modelling results for these gases, such as shown in Fig. 1-3 and 10-12 for Ar, can be found elsewhere.<sup>17</sup>

Inspection of the  $I_B/I_C$  ratios (Fig. 4b) for XeCl in He and Ne indicates that transfer is much slower in these bath gases than in Ar. In addition, the XeCl(B,C) vibrational distributions relax much slower in He and Ne than in Ar. For example at 30 torr of He the distributions are less relaxed than in 2 torr of Ar. Before discussing the He and Ne results, it is necessary to make a few comments concerning the deduction of  $P_{ij}^R$ . For the Ar case sufficient changes in the vibrational distributions occur at rather low pressures so that the effects of just a few collisions with the bath gas can be observed and the  $P_{ij}^R$  elements can be assigned with some confidence, i.e. the parameter  $b$  was determined with some reliability. For He or Ne, on the other hand, pressures of 10-20 torr are required to see significant changes in the distributions and small changes in energy with large cross-sections are difficult to distinguish from larger changes with smaller cross-sections. It is impossible to simultaneously determine  $P_{ij}^R$  and the inelastic collision cross-section with reliability. For C-B transfer this situation is alleviated because the  $I_B/I_C$  ratio identified the cross-section (or magnitude of  $k_T$ ) and the model for  $P_{ij}^T$  can be determined more reliably.

For He and Ne we used the same general form for  $P_{ij}^T$  and  $P_{ij}^R$  as for the Ar case and varied the parameters until a successful fit to the data was found. The best transfer model for He was with  $C = 0.2$ ,  $f = 0.9$  and  $T_i = 0.15$  with  $T_2-T_4$  the same as for Model C and a collision diameter of 4 Å. This gave  $k_T$  of 0.5-1.8, 1.8-2.5, and  $2.5-2.5 \times 10^{-11} \text{ cm}^3 \text{ molec}^{-1} \text{ sec}^{-1}$  for the low, mid, and high v ranges, respectively. For vibrational relaxation a range of parameters could be used with nearly equal success. For example, with  $R_2-R_4$  the same as for model C, successful fits were obtained with  $b = 0.1-0.5$  and  $R_1 = 0.05-0.2$ . However, the best overall fit was judged to be for  $b = 0.3$  and  $R_1 = 0.11$  and these values were adopted for the best fit to the He data. These gave  $k_R = 0.15-1.1$ , 1.1-2.5, and  $2.5-4.4 \times 10^{-11} \text{ cm}^3 \text{ molec}^{-1} \text{ sec}^{-1}$  for the low, mid, and high v ranges.

The neon results were much the same as for He. Relaxation again cannot be determined accurately and several models could fit the experimental results satisfactorily. The best model (E) used  $R_i = 0.3, 0.01, 1.0-0.3$ ,  $T_i = 0.3, 0.01, 0.7, -0.5$  for  $i = 1$  to 4 and  $b = 0.2$ ,  $c = 0.15$  and  $d = 0.87$  with a collision diameter of 5 Å. These parameters gave  $k_T = 0.73-2.6$ , 2.6-3.5, and  $3.5-3.5 \times 10^{-11} \text{ cm}^3 \text{ molec}^{-1} \text{ sec}^{-1}$  and  $k_R = 0.48-2.9$ , 2.9-6.2 and  $6.2-9.5 \times 10^{-11} \text{ cm}^3 \text{ molec}^{-1} \text{ sec}^{-1}$  for the low, mid and high v ranges, respectively.

#### V-B. XeCl(high v) in Krypton, Xenon and Nitrogen

In these bath gases the relaxation and transfer rates are faster than in Ar. The simulated distributions could be represented by a high temperature Boltzmann distribution at pressures as low as  $\sim 5$  torr. The problems encountered in assigning the relaxation rate constants for He and Ne are not present here because significant changes in the distributions are observed below 1 torr and both  $P_{ij}^T$  and  $P_{ij}^R$  can be assigned in a straight forward way. For Kr we used the same model that was developed for the argon case. The best parameters are  $b = 0.5$ ,

$C = 0.5$ ,  $f = 0.8$  and  $R_i = 0.2, 0.01, 1.0, 0.3$  and  $T_i = 1.1, 0.1, 0.7, -0.5$  for  $i = 1$  to 4 and with a collision diameter of  $7\text{ \AA}$ . These gave  $k_R = 0.6 - 2.7, 2.7 - 5.5$ , and  $5.5 - 7.3 \times 10^{-11} \text{ cm}^3 \text{ molec}^{-1} \text{ sec}^{-1}$  and  $k_T = 2.9 - 11.0, 11.0 - 15.5$ , and  $15.5 - 15.5 \times 10^{-11} \text{ cm}^3 \text{ molec}^{-1} \text{ sec}^{-1}$  for the low, mid and high  $v$  ranges. The Kr transfer rate constants are only slightly larger than for Ar which is consistent with the  $I_B/I_C$  ratios in Fig. 4b. However, the relaxation rate constants are significantly smaller than for Ar and, in fact, are even less than for Ne. Yet the observed overall rate of vibrational relaxation is faster in Kr than in Ar because more vibrational energy is lost per collision. Efforts were made to use a model with smaller loss and larger  $k_R$  to fit the Kr results but the fit to the simulated distributions was not as good as for Model F.

Xenon data could not be obtained using the flowing afterglow or resonance absorption method because these methods fail for high Xe pressures. Instead XeCl\* emission was obtained in the presence of Xe bath gas by flowing a  $\sim 1\%$  Cl<sub>2</sub> mixture in Xe through a pulsed discharge and observing the XeCl\* emission directly in the discharge; the details will be reported elsewhere.<sup>18</sup> This method is not specific in the excitation mechanism; i.e. XeCl\* formation may result from Xe(6s) and Xe<sup>\*\*</sup> Rydberg state atoms reacting with Cl<sub>2</sub> or possibly even ion-ion combination. Furthermore, changing the Xe pressure may alter the distribution of excitation mechanisms. Preliminary interpretations<sup>18</sup> indicate that the reaction of Cl<sub>2</sub> with Xe<sup>\*\*</sup> Rydberg states is an important mechanism for the discharge source because the initial vibrational distribution is much broader than the one from the Xe(<sup>3</sup>P<sub>2</sub>), reactions. Although a detailed analysis of the vibrational relaxation and transfer in Xe will have to await a fuller understanding of the excitation mechanism, we estimate from the  $I_B/I_C$  in Fig. 4b that  $k_T \sim 15-20 10^{-11} \text{ cm}^3 \text{ molec}^{-1} \text{ sec}^{-1}$  for XeCl (high  $v$ ) + Xe. The vibrational relaxation resembles the Kr case with (possibly) even more vibrational energy lost per collisions.

The quality of the experimental data for XeCl\* in N<sub>2</sub> was poor and no detailed calculations were performed. However the appearance of the spectra as a function of N<sub>2</sub> pressure closely resembles the Kr bath gas case. The I<sub>B</sub>/I<sub>C</sub> ratio (Fig. 4b) is also similar to Kr. Although no quantitative results can be given it appears that the magnitude of the rate constants and the form of  $\tilde{\chi}$  for N<sub>2</sub> should be quite similar to that for Kr.

## VI. DISCUSSION

### VI.A. Reliability of Rate Constants and Models

Before interpreting our results in terms of molecular interactions, it is necessary to assess their accuracy. The most important variable affecting the magnitude of the rate constants is the lifetimes used in the calculations. Since these are only good to  $\sim 30\%$  and since the population distributions are uncertain to  $\pm 10\%$ , the magnitude of the rate constants are no better than  $\pm 40\%$  on an absolute basis. The relative values should be better than this. In general the k<sub>T</sub> should be more reliable than k<sub>R</sub> for two reasons: 1) the experimental I<sub>B</sub>/I<sub>C</sub> defines the magnitude of k<sub>T</sub> and 2) the simulated distributions of the B state are more reliable than for the C state. Thus, modeling the B state distribution while simultaneously fitting the I<sub>B</sub>/I<sub>C</sub> ratio in the low pressure regime provides a reliable estimate for k<sub>T</sub> (high v). Of course, relaxation and transfer are not independent and, since k<sub>T</sub> depends on vibrational level, the rate at which C relaxes will have an effect on the rate of transfer. This was noted previously with Model B, which overestimated k<sub>R</sub> in the mid v range causing fast vibrational relaxation and consequently the transfer rate decreased too quickly. Nevertheless, the  $\sim 40\%$  estimate should provide a reliable limit to the accuracy of our results for k<sub>T</sub> and k<sub>R</sub>. The values for k<sub>T</sub> (high v) deduced from modeling agree favorably with the estimates from a two state model (section II) affirming that the high v level assignments must be reasonably reliable.

With the above comments held in mind, a glance at Table 2 reveals the following

points:

- (1) The  $k_T$  increase in the order He < Ne < Ar < Kr < N<sub>2</sub> ~ Xe.
- (2) The  $k_R$  increase in the same order except for Kr (and possibly Xe).
- (3) Both  $k_R$  and  $k_T$  depend on vibrational level, increasing in magnitude with increasing v.
- (4) The sum of  $k_R + k_T$  is nearly gas kinetic in magnitude for the high v.
- (5) As the bath gas becomes heavier,  $k_T$  becomes increasingly important relative to  $k_R$  and dominates for Kr (at v?). Fig. 13 shows a plot of  $z P_{ij}^R$  (state to state rate constants) vs.  $\Delta E$  for Model A,  $z P_{ij}^R$  and  $z P_{ij}^T$  for Models B and C for v = 108, 60 and 20. For v = 108, the magnitude of  $z P_{ij}^R$  is similar for Models A and B. The slight difference in shape is due to inclusion of the  $1/\Delta E$  term in Model A.

Because of the large number of vibrational levels and multiple collisions involved in a steady-state system, unique solutions to  $P_{ij}^R$  and  $P_{ij}^T$  are not possible. However, the models we developed for  $P_{ij}^T$  and  $P_{ij}^R$  are useful for contrasting the relaxation and transfer in the various bath gases. Time resolved studies would be required to obtain better transition probability matrices.

It is evident from Fig. 14 that the mean energy loss per transfer collision is greater than for relaxation; however the variation of  $P_{ij}^T$  with  $\Delta E$  is nearly the same as  $P_{ij}^R$  for  $\Delta E \geq 0.15 E_j$ . An exponential gap model could not be used to fit transfer. For  $\Delta E \leq E_j$  it was necessary to reduce the transfer in this  $\Delta E$  range so that the B vibrational distribution would relax fast enough and still match the  $I_B/I_C$  ratio. However, the bulk of the transfer takes place with  $\Delta E$  similar to relaxation.

In Fig. 15 the difference in  $P_{ij}^R$  and  $P_{ij}^T$  for He and Kr are contrasted. As can be seen, the results are quite different for the two bath gases. Both transfer and relaxation in Kr involves loss of large amounts of vibrational energy and significant probability for large quantum transitions. In He the  $P_{ij}^R$  and  $P_{ij}^T$  are grouped more sharply around the initial level. Both Ne and Ar lie between the

extremes for He and Kr.

#### VI. B. Interpretations of Models.

Before discussion of rare gas - XeCl interaction potentials our results will be compared with pertinent data in the literature. Most studies of vibrational relaxation in diatomic molecules have focused on low vibrational levels where the spacing between levels,  $\Delta E$ , is greater than  $kT$ . In the present case the inelastic cross sections are large and the  $\Delta E < kT$ . For this reason we compare our results with vibrational deactivation of KBr<sup>+</sup> (+ represents vibrational excitation) formed from K + Br<sub>2</sub>. The relaxation of KBr seems an ideal choice for several reasons: 1) reaction of Xe\* + Cl<sub>2</sub> is in many ways<sup>5</sup> similar to K + Br<sub>2</sub> and both XeCl\* and KBr have  $\langle E_v \rangle$  of  $\sim 40$  kcal mole<sup>-1</sup>, 2) both KBr and XeCl\* are ionic in nature, and 3) an extensive amount of work has been reported on the vibrational deactivation of KBr. Fisk and coworkers studied KBr relaxation via observation of inelastic scattering of KBr for several collision partners.<sup>19</sup> In addition both trajectory studies of KBr + Ar<sup>20</sup> vibrational relaxation and an information theoretic analysis of experimental data have been reported.<sup>21</sup> We first compare our results with their data by the information theoretic approach. Since KBr was studied by beam techniques, the experimental data consists of the flux density of scattered KBr as a function of center of mass scattering angle and relative velocity.<sup>19</sup> The information theoretic analysis of Crim and Fisk<sup>21</sup> compared the measured translational energy distribution,  $P(f_T)$ , where  $f_T$  is the fraction of initial energy appearing as product translational energy, with a prior of reference distribution,  $P^*(f_T)$ . The appropriate prior for diatomic-atomic collisions in the rigid rotor-harmonic oscillator limit is

$$P^*(f_T) = A_T f_T^{1/2} (1-f_T) \quad (20)$$

where  $A_T$  is a normalization constant.

Apparently  $P(f_T)$  was obtained by averaging over the experimentally observed center of mass angular range ( $\sim 45$  to  $80^\circ$ ).<sup>21</sup> Since there is a significant correlation between the scattering angle and the KBr translational velocity distribution, these "average" experimental distributions may not be good representations of the total distribution. However the reported distributions are clearly two component with one component (the larger) centered around the elastic limit and the second centered around a large inelastic transfer. These two components give two linear regions on the surprisal plot.<sup>21</sup>

To facilitate the comparison, we give our results in a similar manner. Because the initial internal energy of XeCl\* is large ( $E_{mp} \sim 40$  kcal/mole for  $Xe^* + Cl_2$ ), the total energy of the rare gas + XeCl\* collision is approximately fixed. Furthermore if vibrational to translational inelasticity is the dominant deactivation mechanism,  $f_T$  for  $P_{ij}$  is given by

$$f_T = \frac{E_j - E_i}{E_j + kT} \quad (21)$$

The distributions  $P(f_T)$  and  $P^*(f_T)$  for various bath gases are shown in Fig. 15 for XeCl ( $v=100$ ) along with the surprisal  $I(f_T)$ .

$$I(f_T) = -\ln [P(f_T)/P^*(f_T)] \quad (22)$$

If the surprisal is linear, the departure of  $P(f_T)$  from  $P^*(f_T)$  can be described by a parameter  $\lambda$  where,  $\lambda = \frac{dI(f_T)}{d(f_T)}$ .

If  $\lambda=0$ , relaxation takes place statistically while a positive or negative  $\lambda$  indicates relaxation occurs transfer of more or less than the statistical amount of energy, respectively. As can be seen from Fig. 15, the surprisals are linear for He and Ne but deviate from linearity for Ar and Kr. However, a linear plot can be forced and the  $\lambda$  values given in Table 3 range from 17.6 for He to 1.5 for Kr. In Fig. 13 it was shown that Model A and B predict  $P_{ij}^R$  which deviate slightly from each other. This deviation is largest for large  $\Delta E$  transitions

(i.e. large  $f_T$ ) and consequently the surprisals shown in Fig. 15 should be regarded as uncertain in this region. Hence the linear surprisal parameters were obtained only from points with  $f_T < 0.7$ . All of the surprisals show a marked difference (positive deviation) from the statistical case. A similar analysis for  $P_{ij}^T$  gave the same qualitative trends for the bath gases but with  $\lambda$  reduced by a factor of  $\sim 2$  relative to  $P_{ij}^R$ . The large positive  $\lambda$  for He indicates collisions with XeCl\* are nearly elastic, i.e. little energy is transferred from XeCl\* into transition. Collisions with Kr however distribute large amounts of initial vibrational energy into translation and bring about rapid equilibration of translational and internal degrees of freedom. Although modeling was not attempted for Xe as the bath gas, the trends evident in Table 3 would predict that Xe - XeCl\* collisions bring about a statistical or near statistical exchange of energy.

The results of the surprisal analysis are contrasted in Table 3 with the results of vibrational relaxation of KBr. As already noted Crim and Fisk<sup>21</sup> found two linear regions in their surprisal plot for inelastic scattering of KBr. The component at low  $f_T$  gave a large  $\lambda$  consistent with nearly elastic scattering and the  $f_T > 0.2$  component gave  $\lambda \sim 0$  which corresponds to nearly statistical redistribution of energy. The  $I(f_T)$  in Figure 15 for Ar and Kr also could be approximated by a two component distribution similar to that found for KBr. The distributions of Crim and Fisk strongly resemble the sum of an exponential  $P_{ij} \propto e^{-\Delta E_{ij}/b}$  and linear,  $P_{ij} \propto a\Delta E_{ij}$ , distribution. However, theirs is much more extreme form than our model A. We must conclude that, although the two transition probability models are qualitatively similar, they differ significantly at the quantitative level. This disagreement could be a consequence of the lack of inclusion of all scattering angles in the beam studies, the difficulty in obtaining single collision transition probabilities from our steady-state experiments, or a real difference as a consequence of the different intermolecular potentials (see next section) for KBr and XeCl + rare gas.

Included in Table 3 are the mean energy loss collisions for XeCl relaxation and transfer and for KBr relaxation. For Ar and Kr, the  $\langle \Delta E \rangle$  for XeCl is the order observed for KBr deactivation. However, Ne appears to deactivate KBr much more efficiently than XeCl\*. In fact Ne appears to deactivate KBr more efficiently than Ar, which is contrary to what one would expect. Simple theory as well as experimental evidence indicate that for efficient coupling, the collision time and the vibrational period of the oscillator should be closely matched. For light molecules in low vibrational levels with large vibrational frequencies, this results in lighter gases, eg. He, being more efficient for vibrational relaxation. For KBr or XeCl\* in high vibrational levels, the oscillator frequency is small and slower collisions may be more efficient for deactivation. The mean collision time  $\tau_c$  was estimated for an interaction length of  $\sim 2 \text{ \AA}$  and the mean velocity at 300K,  $\bar{v} = (8kT/\pi\mu)^{1/2}$ . For XeCl\*(v=100) the vibrational period  $\tau_v$  is  $\sim 4.5 \times 10^{-13} \text{ sec}$ , and  $\tau_c/\tau_v$  is  $\sim 0.3, 0.5, 0.7, 1.0,$  and 1.1 for He, Ne, Ar, Kr, and Xe, respectively. The match of  $\tau_c$  and  $\tau_v$  is best for Kr and Xe which is consistent with larger  $\langle \Delta E \rangle$  results in Table 3. Of course, the interaction potentials also are more attractive for the heavier rare gases.

In an effort to determine the features of the interaction potential that were important to KBr vibrational deactivation, Matzen and Fisk performed a classical trajectory study for the KBr + Ar system<sup>20</sup> using three different potentials,

Surface I, the best surface was constructed empirically from the two-body interactions of  $K^+$ ,  $Br^-$  and Ar and an Ar-KBr interaction term. Surface II was like Surface I but ignored all attractive interactions. Surface III was similar to II but substituted a spherically symmetric attractive part for the Ar + KBr interaction. The major differences in the potentials were the attractive interactions. Surface II was purely repulsive while the attractive features of I and II were of the same strength but of different shape. On I the incoming Ar is attracted preferentially to the  $K^+$  end of KBr while in III the interaction is symmetric.

The results and conclusions of the trajectory study which are pertinent to XeCl\* relaxation can be summarized as follows:

- i) Both the shape and strength of the attractive interactions were important. Surface I gave the best agreement with experimental results and the calculated distribution did have a two component nature.
- ii) The strength of the attractive interaction determined the magnitude of the inelastic cross-section and both I and III gave higher calculated cross sections than II.
- iii) The shape of the attractive potential was important in determining the average amount of energy transferred. For KBr + Ar, collisions with the K<sup>+</sup> end resulted in larger inelasticities than collisions with the Br<sup>-</sup> end and surface I, which attracted the incoming Ar to the K<sup>+</sup> end of KBr, gave larger inelasticities.
- iv) The high energy component was associated with strong repulsive interactions. Although attractive interactions were important in bringing the collision partners together, large inelasticity was shown only for trajectories which sampled the strongly repulsive regions of the potential energy surface.

The XeCl situation will be more complicated than for KBr - Ar because of multiple surfaces with differing degrees of attractive and repulsive character and because of the coupled vibrational relaxation and electronic state transfer channels.

Although accurate potentials are not known for  $\text{XeCl}^*$  - Rg, qualitative features can be estimated from ab-initio<sup>23</sup> and diatomic-in-molecules<sup>24</sup> calculations which have been reported for some homonuclear trimer systems,  $\text{Rg}_2\text{X}$  (Rg = Ar, Kr and X = F, Cl). The three lowest states of  $\text{Rg}_2\text{X}$  are covalent and repulsive and correlate to  $\text{RgX(A or X)}$  and  $\text{Rg}$ ; these states are of no importance here. The next three higher states are ionic in nature and bound relative to  $\text{Rg}_2^+ + \text{X}^-$ . Only the lowest ionic state ( $2^2\text{B}_2$  in  $\text{C}_{2v}$  geometry) though, is bound with respect to  $\text{RgX}^* + \text{Rg}$ . The most stable geometry of this lowest ionic state is an isosceles triangle. For the mixed rare gas trimers, such as  $\text{RgXeCl}$ , the above potentials will be altered somewhat. First, the isosceles triangle geometry will be distorted with the Rg atom drawn closer to the Xe end of  $\text{XeCl}$ . Secondly,  $\text{RgXeCl}$  trimers would be expected to be much less strongly bound than  $\text{Xe}_2\text{Cl}$ , paralleling the decreasing binding energy of  $\text{RgXe}^+$  vs  $\text{Xe}_2^+$ . In fact, emission from both  $\text{Xe}_2\text{Cl}^*$  and  $\text{KrXeCl}^*$  have been observed.<sup>25,26</sup> Of the lighter  $\text{RgXeCl}^*$ , only  $\text{ArXeCl}^*$  would be (possibly) weakly bound by more than van der Waals forces. According to the calculations, the bound  $\text{Rg}_2^+\text{X}^-$  state correlates with  $\text{RgX(C)}$  and the next higher ionic ( $3^2\text{B}_2$  in  $\text{C}_{2v}$  or  $4^{\prime}\text{A}'$  in  $\text{C}_s$  geometry) state with  $\text{RgX(B)}$ . The approach of Rg to  $\text{XeCl(C)}$  in  $\text{C}_s$  geometry gives an  $\text{A}'$  and an  $\text{A}''$  state (neglecting spin-orbit interaction) depending on whether the sideways approach of Rg to  $\text{XeCl}$  is head on or perpendicular to the singly occupied  $\pi$  orbital. The approach of Rg to  $\text{XeCl(B)}$  gives only an  $\text{A}'$  state as shown in Fig. 16. If the C state is higher in energy than the B state, this results in a curve crossing which can lead to collisional coupling of  $\text{RgX(B,C)}$ . Since  $\text{XeCl(C)}$  is actually lower in energy than  $\text{XeCl(B)}$ , the Rg +  $\text{XeCl(C)}$  potential should correlate adiabatically to the lowest ionic state of  $\text{RgXeCl}^*$  ( $3^2\text{A}'$  in  $\text{C}_s$  geometry) as shown in Fig. 16a. The Rg +  $\text{XeCl(B)}$  potential is repulsive and the interaction of the two  $\text{A}'$  states should be small and collisional mixing of  $\text{XeCl}^*(B,C)$  should be slow, which is contrary to observation. However, the ab initio calculations show

that the collinear approach of  $Rg$  to  $RgX^*$  is also attractive, although the binding is not as large as for the  $C_s$  approach, as shown in Fig. 16. In this case approach of  $Rg$  to  $XeCl(B)$  is attractive, while  $Rg + XeCl(C)$  is repulsive. However the states are of different symmetry and coupling of  $XeCl(B,C)$  via this approach would also be weak unless spin-orbit interaction is included. For such heavy atoms as Kr or Xe this could be of importance and lead to mixing of  $XeCl(B,C)$ . Even though spin orbits effects allow mixing of  $XeCl(B,C)$  the efficiency of this transfer is still surprising. Furthermore, the rapid B-C transfer holds for all  $RgX$  molecules<sup>3,4</sup> regardless of the B and C state ordering and the magnitude of the spin-orbit interactions. Thus, the asymptotic properties of Fig. 16 are not critical for highly vibrationally excited molecules (they may well be of importance for  $v=0-5$  levels when the transfer rates are 1-2 orders of magnitude smaller). Fig. 16 also portrays the behavior of the adiabatic potentials as a function of  $\alpha$ , the angle between the  $Rg - Rg - X$  bonds. As  $\alpha$  increases from  $\sim 60^\circ$  to the linear configuration,  $180^\circ$ , the  $3 A'$  and  $4 A'$  give rise to an avoided crossing. This crossing will exist for all  $RgX^* + Rg$  and presumably is responsible for electronic state transfer. Apparently the large amplitude motion on the potential curves by highly vibrationally excited  $RgX^*$  will lead to frequent sampling of this region where the potentials interact. Furthermore, collisions of both  $RgX(B)$  and  $RgX(C)$  can sample the lowest potential depending on the approach angle of  $Rg$ .

The KBr - Ar trajectory study found that the strength of the attractive interaction determined the magnitude of the inelastic cross sections. This behavior is generally followed here for He - Ar. However, for Kr the relaxation rate constants were much slower with C-B transfer dominating. Only for Kr (and Xe) would the  $3 A'$  potential be significantly bound and transfer may dominate over relaxation for this reason.

Simple theory would predict that Ar striking the K<sup>+</sup> end of KBr would result in larger inelasticities than Ar striking the Br<sup>-</sup> end because K<sup>+</sup> is much lighter than Br<sup>-</sup>. In XeCl\* the attraction is to the Xe<sup>+</sup> end rather than the lighter Cl<sup>-</sup> and our results show somewhat smaller inelasticity for Ar or Ne than in KBr. Because of the stronger attractive interactions and presumably softer repulsions for XeCl\* the present results suggest that the attractive interactions play a more dominant role in XeCl\* + Rg than KBr + Rg. Greene et al,<sup>27</sup> in studying the inelastic scattering of CsI by Ar and Xe suggest that short lived complex may be formed at low collisions energies. Their results fit statistical partitioning of the total energy. Greene et al<sup>27</sup> also suggest that in the interaction of a highly excited ionic molecule, such as KBr or CsI with Ar, that during the bond extension prime of the vibration the interaction may resemble Ar interacting with K<sup>+</sup>. Such an interaction is much stronger than with the molecule leading to stronger attractive interaction during the collision. For XeCl\* + Rg this effect will be enhanced because RgXe<sup>+</sup> is chemically bound (at least for Rg = Kr,Xe) whereas in ArK<sup>+</sup> the attraction is only electrostatic in nature. We see some evidence for this because of the dependence of the rate constants on vibrational excitation. For the high v the attractive interaction is stronger and leads to larger inelastic cross sections as opposed to the low v levels where the interaction is more like the weaker Rg-XeCl interaction.

## VI. Conclusions

From computer simulation of the XeCl(B-X) and XeCl(C-A) bound-free emission spectra in He, Ne, Ar, and Kr bath gases, the vibrational and electronic state distributions were assigned for a range of pressures. State-to-state rate constants for vibrational relaxation and electronic state transfer have been assigned for XeCl\*(B,C) + Rg collisions by master equation calculations fitting the variation of the vibrational distributions with Rg pressure. The electronic state transfer rate constants for the v = 70-130 range varied from  $15-2.5 \times 10^{-11} \text{ cm}^3 \text{ molec}^{-1} \text{ sec}^{-1}$  for the Kr-He series; the

the vibrational relaxation rate constants are comparable with the exception of Kr which is smaller than for Ar. The magnitude of both the relaxation and transfer rate constants decline by an order of magnitude from  $v=100$  to  $v = 10$ . The model for state-to-state vibrational relaxation is adequately represented by the exponential gap law. For electronic state transfer the change of vibrational energy is larger than for the collisions giving vibrational relaxation without change in electronic state, and the model is Poisson in nature. The larger loss of vibrational energy associated with electronic state changing collisions is explained by the attractive potential involved in interconversion of the XeCl(B) and XeCl(C) states.

#### Acknowledgments

This work was supported by the Advanced Research Projects Agency of the U.S. Department of Defense (monitored by ONR-N00014-76-0380) and by the U.S. Department of Energy DE-AC02-80ET33068. TDD thanks Phillips Petroleum for a research fellowship. We thank Dr. H. C. Brashears for providing most of the XeCl\* spectra from the Xe( $^3P_1$ ) reactions.

## References

1. A. Brau in: Excimer lasers, Topics in Applied Physics, Vol. 30, ed. C. K. Rhodes (Springer, Berlin, 1979).
2. a) W. K. Bischel, H. H. Nakano, D. J. Eckstrom, R. M. Hill, D. L. Huestis, and D. C. Lorents, App. Phys. Lett., 34 565 (1979).  
b) R. Burnham, App. Phys. Lett., 35, 48 (1979).
3. a) L. A. Gundel, D. W. Setser, M. A. A. Clyne, J. A. Coxon, and W. Nip, J. Chem. Phys., 64, 4390 (1976).  
b) J. E. Velazco, J. H. Kolts, and D. W. Setser, J. Chem. Phys. 65, 3468 (1976).  
c) J. E. Velazco, J. H. Kolts, and D. W. Setser, J. Chem. Phys. 69, 4357 (1978).  
d) C. H. Chen, M. C. Payne, G. S. Hurst, and J. P. Judish, J. Chem. Phys. 65, 4028 (1976).
4. a) J. H. Kolts and D. W. Setser, J. Phys. Chem., 82 1766 (1978). The <sup>17</sup>F data (B/C ratios) presented in this paper are incorrect: for the pressure shown the correct results closely resemble those of KCl.  
b) J. H. Kolts, J. E. Velazco, and D. W. Setser, J. Chem. Phys., 71 1247 (1979).  
c) K. Tamagake, D. W. Setser, and J. H. Kolts, J. Chem. Phys. In press (1981).
5. a) K. Tamagake and D. W. Setser, J. Chem. Phys. 67, 4370 (1977).  
b) K. Tamagake, J. H. Kolts, and D. W. Setser, J. Chem. Phys. 71, 1264 (1979).  
c) D. W. Setser, T. D. Dreiling, H. C. Brashears, Jr., and J. H. Kolts, Faraday Disc. Chem. Soc. 67, 255 (1979).
6. M. F. Golde and A. Kvaran, J. Chem. Phys. 72, 434, 442 (1980).
7. H. C. Brashears and D. W. Setser, J. Phys. Chem., 84 224 (1980).
8. P. J. Marcoux, M. van Swaay, and D. W. Setser, J. Phys. Chem., 83, 3168 (1979).

9. The correct expressions (for the calculations of ref. 5b) for the A-potential and transition moment should read  $V(R)^{A,3/2} = 1.786 \times 10^7 \exp(-2.8821 R')$ ,  $\mu(R) = 70.8 \exp(-1.424 R')$  with  $R'$  given in the text. The original expressions in ref. 5b were obtained by neglecting the  $(R-R_e')^2$  term in the expression for  $R'$ .
10. a) P. J. Hay and T. H. Dunning, J. Chem. Phys., 69 2209 (1978).  
b) T. H. Dunning and P. J. Hay, J. Chem. Phys. 69, 434 (1978).
11. M. C. Castex, J. LeCalve, D. Haaks, B. Jordan and G. Zimmerer, Chem. Phys. Lett. 70, 106 (1980).
12. a) E. D. Poliakoff, S. H. Southworth, M. G. White, G. Thornton, R. A. Rosenberg, and D. A. Shirley, J. Chem. Phys. 72, 1786 (1980).  
b) G. P. Quigley and W. M. Hughes, Appl. Phys. Lett., 32 627 (1978).
13. D. W. Setser, H. C. Brashears, and T. D. Dreiling, J. de Phys., C3 195 (1980).
14. a) J. Tellinghuisen and M. R. McKeever, Chem. Phys. Lett., 72, 94 (1980).  
b) J. Boker and C. K. Rhodes, J. Chem. Phys., 73, 2626 (1980).
15. Y. C. Yu and D. W. Setser, J. Chem. Phys., to be published.
16. W. H. Duewer, J. A. Coxon, and D. W. Setser, J. Chem. Phys., 56 4355 (1972).
17. T. D. Dreiling, Ph.D. Thesis, Kansas State University (1981).
18. D. W. Setser and J. K. Ku, to be published.
19. a) M. S. Chou, F. F. Crim, and G. A. Fisk, Chem. Phys. Lett., 20 464 (1978).  
b) T. Donohue, M. S. Chou, and G. A. Fisk, Chem. Phys. 2 271 (1973)  
c) F. F. Crim, M. S. Chou, and G. A. Fisk, Chem. Phys. 2 283 (1973).  
d) F. F. Crim, H. B. Bente, and G. A. Fisk, J. Phys. Chem., 78 2438 (1974).
20. M. K. Matzen and G. A. Fisk, J. Chem. Phys., 66 1514 (1977).
21. F. F. Crim and G. A. Fisk, J. Chem. Phys., 65 2480 (1976).
22. See for example J. I. Steinfeld, 64 17 (1967) with application to  $I_2$  ( $B^{3\Pi}_{o,u}$ ,  $v=25$ ).
23. W. R. Wadt and P. J. Hay, J. Chem. Phys. 68 3850 (1978).

24. D. C. Huestis and W. E. Schulotter, J. Chem. Phys. 69 3100 (1978).
25. F. K. Tittel, W. C. Wilson, R. E. Stickel, G. Marowsky, and W. E. Ernst, Appl. Phys. Lett. 36 405 (1980).
26. H. C. Brashears, D. W. Setser, and Y. C. Yu, J. Chem. Phys. 74 10 (1981).
27. E. F. Greene, R. B. Hall, and N. A. Sondergaard, J. Chem. Phys. 66 3171 (1977).

Table 1. XeCl Energy Levels and Radiative Lifetimes

Vibrational Level	C state		B state	
	Energy (cm <sup>-1</sup> )	$\tau$ (nsec)	Energy (cm <sup>-1</sup> )	$\tau$ (nsec)
0	139.42	120.0	369.42	11.0
4	876.08	127.6	1136.05	11.08
8	1590.86	136.4	1882.33	11.88
12	2284.25	137.2	2608.63	12.29
16	2956.77	142.8	3315.38	12.64
20	3608.94	146.9	4002.98	12.53
24	4241.29	152.3	4671.84	12.35
28	4854.33	174.1	5322.39	13.43
32	5448.6	182.1	5955.05	14.10
36	6024.61	195.3	6570.25	14.50
40	6582.89	195.5	7168.42	14.84
44	7123.96	210.3	7750.00	16.12
48	7648.33	224.6	8315.41	16.38
52	8156.52	230.6	8865.10	17.25
56	8649.03	245.0	9399.49	18.69
60	9126.35	256.4	9919.03	19.33
64	9588.98	265.0	10424.17	20.15
68	10037.4	275.2	10915.27	21.35
72	10472.1	279.1	11392.77	22.42
76	10883.4	270.2	11897.07	23.88
80	11302.0	296.2	12308.67	24.78
84	11698.1	298.2	12747.97	26.04
88	12082.3	308.3	13175.27	27.52

Table 1., Continued

Vibrational Level	C state		B state	
	Energy (cm <sup>-1</sup> )	τ (nsec)	Energy (cm <sup>-1</sup> )	τ (nsec)
92	12454.9	318.1	13590.97	28.98
96	12815.3	325.6	13995.47	30.21
100	13167	337.7	14389.17	31.77
104	13507.3	343.3	14772.37	33.21
108	13837.6	349.1	15145.147	35.14
112	14158.1	352.8	15508.67	37.16
116	14469.3	357.9	15862.27	39.03
120	14771.5	375.1	16206.67	40.91
124	15065	398.5	16541.97	
128	15627.1	433.7	17186.47	
136	15896.2	438.5	17496.07	

Table 2. Rate Constant Summary

Bath gas	Model	Model Parameters				$k_R^a$	$k_T^a$					
	b	c	f	$R_1^b$	$T_1^b$	d <sup>c</sup>	low-v <sup>d</sup>	mid-v	high-v	low-v <sup>d</sup>	mid-v	high-v
Ar	A	0.11	-	-	-	-	4.95	4.5-13	13-20	20-34	-	-
	B	0.10	0.10	0.15	1.0	1.2	6.0	2.5-13	13-25	25-35	3.0-11	11-15
	C	0.15	0.2	0.15	0.5	1.2	6.0	1.0-6	6.0-12	-	3.0-11	11.0-15
He	D	0.3	0.2	0.10	0.11	0.15	4.0	0.15-1.1	1.1-2.5	2.5-4.4	0.5-1.8	1.8-2.5
	E	0.2	0.15	0.13	0.3	0.3	5.0	0.5-2.9	2.9-6.2	6.2-9.5	0.7-2.6	2.6-3.5
Ne	F	0.05	0.05	0.20	0.2	1.1	7.0	0.6-7.7	2.7-5.5	5.5-7.3	3.0-11	11.0-16
	Xe	-	-	-	-	-	-	-	-	-	-	~15-20

a. Units of  $10^{-11} \text{ cm}^3 \text{ molec}^{-1} \text{ sec}^{-1}$ ; the  $k_T$  in this table take precedence over all other previous reports in references 5b and 7.

b.  $R_2-R_4$  and  $T_2-T_4$  were the same for all models.  $R_2-R_4 = 0.1, 1.0, -0.3$ , and  $T_2-T_4 = 0.1, 0.7, -0.5$ .

c. Collision diameter in Angstroms used to calculate the collision frequency.

d. The low, mid, and high v represent the ranges v=0-30, 30-70, and 70-130, respectively.

Table 3. Summary of Energy Disposal

Bath Gas	Relaxation		Transfer	
	$\langle \Delta E_R \rangle^a$	$\lambda^b$	$\langle \Delta E_T \rangle^a$	$\lambda^b$
He	2.1	$17.6 \pm 0.4$	5.0	$9.9 \pm 0.3$
Ne	3.0	$11.2 \pm 0.4$	6.4	$6.6 \pm 0.3$
	(~ 15.0) <sup>c</sup>	(24.0, 0.5) <sup>c</sup>		
Ar	5.4	$4.7 \pm 0.4$	8.3	$3.5 \pm 0.3$
	(~ 10.0) <sup>c</sup>	(16.0, 0.8) <sup>c</sup>		
Kr	9.0	$1.5 \pm 0.4$	12.5	$0.4 \pm 0.2$

a. Mean energy loss in kcal/mole for relaxation  $\langle \Delta E_R \rangle = \sum P_{ij}^R \Delta E / \sum P_{ij}^R$ ,  $\langle \Delta E_T \rangle = \sum P_{ij}^T \Delta E / \sum P_{ij}^T$ .

b. Linear surprisal parameter; the error represents std dev. to a least square fit.

c. Second entry in parenthesis refers to the two components of the vibration relaxation of KBr (from Crim & Fisk<sup>21</sup>).

## FIGURE CAPTIONS

- Figure 1.** Comparison of experimental (—) and simulated (---) spectra of the B-X and C-A emission of XeCl resulting from the reaction of  $\text{Xe}^* + \text{Cl}_2$  in Ar. In each case the B-X spectra have been attenuated so that the most intense peak of the C-A and B-X emission have the same height.
- Figure 2.** Same as Figure 1 but from  $\text{Xe}^* + \text{CCl}_4$ . In the 240-260 nm region, the simulated B-X spectra are above the experimental spectra because a flat potential was used for the  $\text{XeCl}(X)$ . The use of a more realistic potential would reduce the intensity by shifting the transition occurring at the inner turning point of the upper state to longer wavelengths.
- Figure 3.** Simulated (---) and experimental (—) spectra from  $\text{Xe}^* + \text{COCl}_2$ . The lack of oscillatory structure, even at low pressure prevents a reliable vibrational distribution from being assigned.
- Figure 4.** Comparison of the  $I_B/I_C$  intensity ratios as a function of pressure for a) The  $\text{Cl}_2$ ,  $\text{CCl}_4$  and  $\text{COCl}_2$  donors in argon and b) for  $\text{Xe}^* + \text{Cl}_2$  in the various bath gases. The dashed line in b serves only as an aid in identifying the argon points.
- Figure 5.** Steady-state  $\text{XeCl}(B,C)$  vibrational distribution obtained from simulation of  $\text{Xe}^* + \text{Cl}_2$  spectra at various Ar pressures. Because of different  $\omega_e$  and  $\omega_{e,e}$  values, the  $v_{\max}$  levels for the two states are different; even if the vibrational energy is the same, see Table 1.
- Figure 6.** Steady-state  $\text{XeCl}(B,C)$  vibrational distribution obtained from simulation of the  $\text{Xe}^* + \text{CCl}_4$  spectra at various pressures of Ar.
- Figure 7.** Steady-state  $\text{XeCl}(B,C)$  vibrational distributions from  $\text{Xe}^* + \text{COCl}_2$  at 0.1-0.2 and 3-6 torr. Only the shapes of the distributions have significance; note the similarity to Boltzmann distributions.

- Figure 8. a) Comparison of  $\text{XeCl}(\text{B-X})$  experimental spectrum with two simulated spectra (--- and ···), which give satisfactory fits. The simulated spectra for the  $\text{Cl}_2$  case are nearly superimposed.  
b) Corresponding vibrational distributions.
- Figure 9. Comparison of simulated distributions (—) and calculated distributions from Model A (---) for the vibrational relaxation of  $\text{XeCl}(\text{C})$  in Ar.
- Figure 10. Comparison of simulated (—) and calculated distributions from Model B (---) of  $\text{XeCl}(\text{B})$  and  $\text{XeCl}(\text{C})$  from  $\text{Xe}^* + \text{Cl}_2$  in Ar. Model B includes both relaxation and transfer processes. The apparent populations in the lowest two levels, which represent the real  $v=0-8$  levels for the higher pressures can not be interpreted literally, see text.
- Figure 11. Comparison of experimental and calculated  $I_B/I_C$  ratios in Ar. For clarity the  $I_B/I_C$  ratios have been moved up 4 and 2 units for  $\text{Cl}_2$  and  $\text{CCl}_4$ , respectively. The calculated results are the dashed lines (best fit) or dotted line. The best fit results are from Model B ( $\text{Cl}_2$ ) and Model C for  $\text{CCl}_4$  and  $\text{COCl}_2$ . The dotted line is a Model B calculation for  $\text{CCl}_4$ ; the poor fit necessitated an improvement and led to Model C.
- Figure 12. Comparison of Model B (···) and Model C (---) results for  $\text{Xe}^* + \text{CCl}_4$  data. The poor fit for Model B required improvement and Model C was developed to fit the  $\text{Xe}^* + \text{CCl}_4$  data (see text).
- Figure 13. Comparison of relative  $z \cdot P_{ij}$  for Model A and B for starting  $v=20$  40, and 108. ● =  $zP_{ij}^R$  (Model A), ■ =  $zP_{ij}^R$  (Model B), and ★ =  $zP_{ij}^T$  (Model B).
- Figure 14. Comparison of  $P_{ij}^T$  (upper panel) and  $P_{ij}^R$  (lower) for He (Model D) and Kr (Model F) as bath gases. To emphasize the differences between the two models, the maximum  $P_{ij}$  have been normalized to 10

Figure 15. Comparison of translational energy distributions  $P(f_T)$  (—) (lower) and the corresponding surprisals (upper), calculated from Eqn. 22 for the various bath gases. Because the calculations included only every fourth level the origin of  $f_T$  is 0.05.

Figure 16. Schematic  $RgRgX^*$  potentials as a function of  $\alpha$ , the  $Rg-Rg-X$  band angle and the separated  $Rg + RgX^*$  states to which they correlate. The potential is drawn for a bound trimer, i.e.  $KrXeCl^*$  or  $Xe_2Cl^*$ . The  $C_{2v}$  geometry is realized only for  $Xe_2Cl^*$ . For the lighter rare gases all the curves become less attractive and finally strictly repulsive in the series  $Ar < Ne < He$ .

